



**Tufts**  
UNIVERSITY

School of  
Engineering

# WIND TUNNEL SIMULATION OF FLOW CONTROL WITH PULSED IMPINGING AIR JETS

A Senior Honors Thesis Submitted by

Reeve Dunne

IN PARTIAL FULFILLMENT OF THE REQUIREMENTS FOR A BACHELOR OF  
SCIENCE IN MECHANICAL ENGINEERING

SCHOOL OF ENGINEERING  
TUFTS UNIVERSITY  
MEDFORD, MA  
MAY 2010

Advisor: Richard Wlezien, Ph.D.

Thesis Committee: Vincent Manno, Sc.D.

## ABSTRACT

The technology of natural laminar flow airfoils presents an opportunity to vastly increase the efficiency of aircraft by decreasing the friction drag on the wing during flight. These airfoils however are much more susceptible to flow separation and stall conditions resulting in increased drag and loss of lift on the airfoil. Flow control represents a possibility to prevent separation on these airfoils allowing them to be used throughout the aeronautics industry. Separation control is achieved by artificially adding momentum to the flow or manipulating disturbances within the boundary layer. Extensive research has been performed investigating the effect of exciting the boundary layer physically or acoustically with mixed success. Significant control has been achieved however with pulses of air injected directly into the boundary layer tangentially with the flow over the airfoil surface.

In this paper the flow control potential of small, pulsed jets impinging on the airfoil surface is investigated experimentally using a wind tunnel. The effect of a single short pulse, generated at several different locations and angles on the airfoil was tested at a separated angle of attack. Using smoke wire flow visualization the effect of the pulse on separation, the wake size and all other characteristics of the flow were determined during and after the pulse passed the surface of the airfoil. The images produced were compared directly and quantitatively using image analysis software. This analysis successfully demonstrated that short duration impinging jets had an immediate effect on attaching the flow, and a long-term effect decreasing overall drag determined from the wake size. Additionally it was shown that the orientation of the jet had a significant effect on the flow behavior, and the shape of the pulse itself. These experiments generated sufficient proof of the efficacy of impinging jets for separation control and determined several highly effective orientations of the jet for as a basis for more quantitative research.

## ACKNOWLEDGEMENTS

I would like to use this opportunity to thank everyone who has helped to guide me through my undergraduate career culminating in this thesis. First of all I would like to thank my thesis advisor Dr. Rich Wlezien, who provided me with the wealth of knowledge necessary to even begin this work, and supported me for two years from the beginnings of constructing the wind tunnel, through the final research presented here. Additionally I would like to thank the other member of my committee and my academic advisor, Dr, Vincent Manno, who provided me with the guidance necessary to complete my undergraduate studies.

Also I would like to thank the machine shop coordinator Jim Hoffman, for his help and expertise in building the experimental setup required for this research. Vincent Miraglia, mechanical engineering coordinator for his help finding equipment throughout Bray Laboratory and all other assistance he provided along the way. The image processing software necessary was made available to me by Dr. Chris Rogers, who with his LabVIEW® programming expertise, and enthusiasm, led me through the entire process. Lastly thank you to the Tufts Mechanical Engineering faculty who have taught and guided me through the past four years. Finally I would like to thank the student team of David Bader, Jess Noble, Robert Berg, Paul Vidich, Tim Roberts and Colin Patterson who helped me construct the wind tunnel, and without whom none of this research would have been completed. Also Ph.D students Alfram Bright and Jenna Eppink who helped me with my research and guided me through the thesis with their experience. Lastly I would like to thank my family whose support gave me the opportunity to study at Tufts, and have continued to help me every step of the way

## TABLE OF CONTENTS

Abstract .....	i
Acknowledgments.....	ii
Table of Contents.....	iii
List of Tables and Figures.....	v
Nomenclature .....	viii
1.0 INTRODUCTION AND MOTIVATION .....	1
2.0 BACKGROUND .....	3
2.1 Laminar Flow Airfoils .....	3
2.1.1 Drag.....	3
2.1.2 Airfoil Design .....	5
2.2 Flow Control .....	7
2.2.1 Passive Flow Control .....	7
2.2.2 Active Flow Control .....	8
3.0 EXPERIMENTAL APPROACH.....	11
3.1 Wind Tunnel .....	11
3.2 Airfoil.....	12
3.4 Air Puffer .....	14
3.5 Flow Visualization.....	16
3.6 Test Methodology .....	19
3.7 Analysis Methodology .....	21
4.0 RESULTS .....	22
4.1 Qualitative Comparison .....	22
4.1.1 Base Airfoil (No Control) .....	22
4.1.2 Streamwise air jets .....	23
4.1.3 Leading Edge Impingement .....	26
4.1.4 45-degree Impinging Jets Above the Leading Edge .....	28
4.1.5 22.5-degree Impinging Jets Above the Leading Edge .....	31
4.1.6 45-Degree impinging jet 1.4 inches behind the leading edge .....	35
4.2 Quantitative Comparison .....	38
6.0 CONCLUSIONS.....	42

6.1 Future Work .....	46
REFERENCES .....	48
ADDITIONAL REFERENCES .....	50
APPENDIX A – AIRFOIL MODEL DRAWINGS .....	51
APPENDIX C—DATA ACQUISITION HARDWARE .....	56

## LIST OF TABLES AND FIGURES

FIG. 2.1	Skin Friction .....	4
FIG. 2.2	Cylinders in Cross Flow .....	5
FIG. 2.3	Airfoil Comparison.....	6
FIG. 2.4	Pressure Distribution .....	6
FIG. 2.5	Vortex Generators .....	7
FIG. 2.6	Boundary Layer Profiles.....	9
FIG. 2.7	Boundary Layer Profiles II.....	10
FIG. 3.1	Wind Tunnel.....	11
FIG. 3.2	Smoke Flow.....	12
FIG. 3.3	NLF(2)-0415.....	13
FIG. 3.4	CL $\alpha$ Graph.....	13
FIG. 3.5	Test Airfoil .....	14
FIG. 3.6	Puffer System .....	15
FIG. 3.7	Configuration 1.....	15
FIG. 3.8	Configuration 2.....	15
FIG. 3.9	Configuration 3.....	16
FIG. 3.10	Configuration 4.....	16
FIG. 3.11	Configuration 5.....	16
FIG. 3.12	28 Gauge Smoke.....	17
FIG. 3.13	Smoke Wire.....	18
FIG. 3.14	Fog Tubing .....	19
FIG. 3.15	SPOT Flash.....	19
FIG. 3.16	Uncontrolled Flow.....	20
FIG. 4.1	Flow Separation.....	22
FIG. 4.2	Drag Polar.....	23
FIG. 4.3	10ms Configuration 1 Pulse I.....	23
FIG. 4.4	5ms Configuration 1 Pulse I.....	24
FIG. 4.5	10ms Configuration 1 Pulse II.....	24
FIG. 4.6	5ms Configuration 1 Pulse II.....	25
FIG. 4.7	5ms Configuration 1 Pulse III .....	25

FIG. 4.8	10ms Configuration 1 Pulse III .....	25
FIG. 4.9	10ms Configuration 2 Pulse I.....	26
FIG. 4.10	20ms Configuration 2 Pulse I.....	26
FIG. 4.11	10ms Configuration 2 Pulse II.....	27
FIG. 4.12	20ms Configuration 2 Pulse II.....	27
FIG. 4.13	Configuration 2 Wake Vortices.....	28
FIG. 4.14	10ms Configuration 3 Pulse I.....	28
FIG. 4.15	10ms Configuration 3 Pulse II.....	29
FIG. 4.16	20ms Configuration 3 Pulse I.....	29
FIG. 4.17	20ms Configuration 3 Pulse II.....	29
FIG. 4.18	20ms Configuration 3 Pulse III .....	30
FIG. 4.19	20ms Configuration 3 Pulse IIII.....	30
FIG. 4.20	10ms Configuration 4 Pulse I.....	31
FIG. 4.21	10ms Configuration 4 Pulse II.....	31
FIG. 4.22	30ms Configuration 4 Pulse I.....	31
FIG. 4.23	20ms Configuration 4 Pulse I.....	32
FIG. 4.24	20ms Configuration 4 Pulse II.....	32
FIG. 4.25	20ms Configuration 4 Pulse III .....	32
FIG. 4.26	20ms Configuration 4 Pulse IIII.....	33
FIG. 4.27	30ms Configuration 4 Pulse II.....	33
FIG. 4.28	30ms Configuration 4 Pulse III .....	34
FIG. 4.29	10ms Configuration 5 Pulse I.....	35
FIG. 4.30	10ms Configuration 5 Pulse II.....	35
FIG. 4.31	10ms Configuration 5 Pulse III .....	36
FIG. 4.32	10ms Configuration 5 Pulse IIII.....	36
FIG. 4.33	20ms Configuration 5 Pulse I.....	36
FIG. 4.34	20ms Configuration 5 Pulse II.....	37
FIG. 4.35	20ms Configuration 5 Pulse III .....	37
FIG. 4.36	30ms Configuration 5 Pulse I.....	38
FIG. 4.37	30ms Configuration 5 Pulse II.....	38
FIG. 4.38	30ms Configuration 5 Pulse III .....	38
FIG. 4.39	Linear Wake Size Comparison I.....	39
FIG. 4.40	Linear Wake Size Comparison II .....	40
FIG. 4.41	Wake Size Comparison Endpoint Fixed I.....	41

FIG. 4.42	Configuration 4 Scatter Plot .....	41
FIG. 4.43	Wake Size Comparison Endpoint Fixed II.....	42
FIG. 4.44	Configuration 5 Scatter Plot .....	42
FIG. A.1	NLF(2)-0415.....	52
FIG. B.1	Test Airfoil Large Half .....	54
FIG. B.1	Test Airfoil Small Half .....	55
TABLE 3.1	Experiments Performed.....	20

## Nomenclature

$A_p$ —Projected Area

$c$ —Airfoil Chord

$C_\mu$ —Momentum Coefficient ( $=\frac{\rho_j U^2_j H}{1/2 \rho_\infty U^2_\infty c}$ )

$C_D$ —Coefficient of Drag ( $=\frac{F_D}{1/2 \rho U_\infty^2 A_p}$ )

$C_f$ —Local Coefficient of Friction

$C_L$ —Coefficient of Lift ( $=\frac{F_L}{1/2 \rho U_\infty^2 A_p}$ )

$F_D$ —Drag Force

$F_L$ —Lift Force

$Re$ —Chord Reynolds Number ( $\frac{\rho U c}{\mu}$ )

$H$ —Characteristic Jet Size (width/diameter)

$U$ —Flow Velocity

$x$ —Streamwise(chordwise) Coordinate

$y$ —Cross Stream Coordinate

$z$ —Spanwise Coordinate

$\alpha$ —Angle of Attack

$\rho$ —density

$\mu$ —Dynamic Viscosity

## Abbreviations

FDM—Fused Deposition Modeling

MEMS—Micro Electrical-Mechanical Systems

ms—Millisecond

NI—National Instruments®

NLF—Natural Laminar Flow

ns—Nanosecond

PIV—Particle Image Velocimetry

SJA—Synthetic Jet Actuator

STP—Standard Temperature and Pressure

## Subscripts

$j$ —Jet Conditions

$\infty$ —Freestream Conditions

## Definitions

**Active Flow Control**—Flow control achieved using oscillatory or pulsing actuation.

**Boundary Layer**—Flow near wall with velocity less than 99% of freestream velocity.

**Closed Loop Control**—Control that utilizes dynamic input (feedback) to adjust actuation real time.

**Laminar Flow**—Flow condition defined by flow in parallel layers with no disruption.

**Open Loop Control**—Control system that is pre-set, with no feedback.

**Passive Flow Control**—Flow control achieved with steady state actuation.

**Separation Point**—Point behind which freestream flow is no longer attached to the airfoil.

**Stall**—sudden decrease in  $C_L$  that occurs when a significant portion of the airfoil is separated.

**Slats**—High Lift devices that project from the front of the airfoil to increase  $C_L$  for takeoff and landing

**Turbulent Flow**—Flow condition defined by random chaotic mixing.

## 1.0 INTRODUCTION AND MOTIVATION

In the modern world aircraft are critical for the transport of people and infrastructure. As a result, increasing the efficiency of large transport aircraft is critical to conserve resources and prevent environmental damage caused by fossil fuels. Therefore there is significant motivation to reduce drag on these aircraft. To date the most promising technology to achieve this reduction is the laminar flow airfoil that allows aircraft wings to maintain laminar flow at much higher Reynolds numbers than usually possible. Laminar flow has significantly lower skin friction which, when applied over a significant surface of the aircraft wing, results in vastly lower drag and higher fuel efficiency. Laminar flow is much more sensitive to flow conditions than turbulent flow. Adverse pressure gradients may immediately trip a laminar flow to turbulence or, if sufficiently powerful will force the flow to separate from the airfoil resulting in significant loss of lift and increase in overall drag. Additionally surface roughness will cause the flow to transition to turbulence prematurely. With composite materials and advanced manufacturing processes aerodynamically smooth surfaces can be fabricated. However high lift devices such as slats that project from the front of the airfoil to increase lift coefficient for takeoff and landing cannot be used because they will cause too much roughness at the leading edge. Another method of generating high lift is necessary for laminar flow to be utilized on large scale aircraft.

Significant research has been performed in flow control that causes the flow to remain attached at much higher angles of attack than possible with standard airfoils. These flow control techniques are usually achieved by blowing air into the boundary layer, sucking air out of the boundary layer or a combination of both. Control can be achieved with pulsed, oscillatory or steady actuation. While previous research has focused on blowing air tangentially within the boundary layer, this work focuses on small jets impinging on the airfoil.

The objectives of this research are to determine what effect impinging jets have on controlling separation. We seek to understand the advantages and disadvantages of impinging jets versus other methods of flow control, most specifically tangential pulsed jets. We wish to understand the effect of the location, angle and duration of the pulse, and lastly what is the best configuration for separation control. In order to test these phenomena wind tunnel experiments were performed with multiple short duration air pulses placed at various angles and positions along an airfoil. Flow visualization was used to generate still images of the flow conditions over

the stalled portion of the airfoil during and after the pulses. These images were qualitatively and quantitatively analyzed to achieve an accurate understanding of the effect of impinging jets.

## 2.0 BACKGROUND

### 2.1 Laminar Flow Airfoils

#### 2.1.1 Drag

On a body immersed in a flow, such as an airfoil, there are two distinct causes of drag; skin friction, or viscous drag, and form or pressure drag. Viscous drag is caused by the friction between the fluid and the body. For laminar flow the skin friction coefficient at any point can be calculated as

$$C_f = .664/\sqrt{Re_x} \quad 2.1$$

which can be integrated over the surface of the airfoil to calculate the total viscous drag coefficient on the airfoil as

$$C_D = 1.33/\sqrt{Re_L}. \quad 2.2$$

For turbulent flow the skin friction coefficient at any point on a flat plate has been shown experimentally to be approximately

$$C_f = .0594/Re_x^{1/5} \quad 2.3$$

for chord Reynolds numbers below  $10^7$ . Integrating this value gives a total drag coefficient based on chord length of

$$C_D = .0742/Re_L^{1/5}. \quad 2.4$$

From these equations it can be shown that at sufficiently high Reynolds numbers the skin friction caused by laminar flow is significantly lower than that of turbulent flow [1]. Figure 2.1 shows a plot of skin friction coefficient versus Reynolds number for all likely flight conditions [2].

In addition to viscous drag objects in real flow generate pressure drag, or form drag caused when the flow does not remain fully attached on the object. This drag is calculated by integrating the pressure difference over the surface of the body.

$$F_D = \int_{surface} p dA \quad 2.5$$

The wake behind the body is defined as the area behind the separation point where the flow is no longer attached to the body. In the wake the velocity and pressure are very low, thus the form drag on the body scales with the size of the wake [1]. The wake size and pressure difference around any shape can be measured experimentally and combined with viscous drag to determine the drag coefficient for the shape. If the flow remains completely attached there is a very small

wake near the trailing edge and therefore very low form drag. However if the flow is separated,

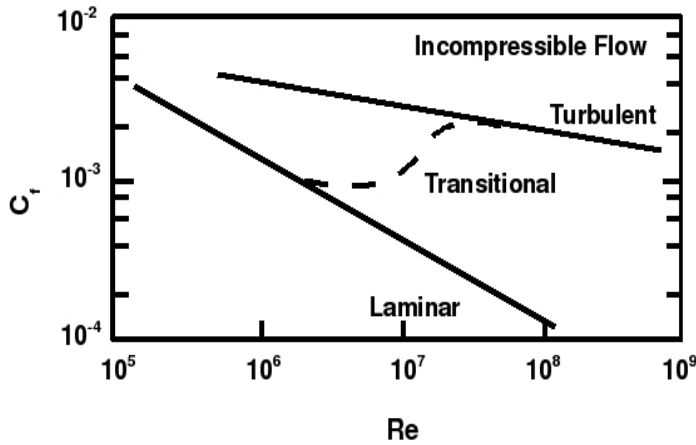


Figure 2.1 Skin friction coefficients for laminar, transitional and turbulent flow as a function of Reynolds number. Note that as Re increases laminar flow has relatively higher efficiency [2].

a very large wake and a high form drag results. The form drag on an airfoil is almost always much higher than the viscous drag. Numerical simulations of the NLF(2)-0415 airfoil at a chord Reynolds number of 25,000 and zero angle of attack result in a drag coefficient of 0.03037. The viscous drag calculated with Equation 2.4 is 0.0098, less than one third of the total drag coefficient. At higher stalled angles of attack such as 8 degrees the overall drag coefficient is 0.064 such that the viscous effects

represent less than one sixth of the total drag [3].

While laminar flow generates less viscous drag, flow in the laminar regime is more susceptible to separation. The primary cause of separation is an adverse pressure gradient generated as the flow moves aft over the airfoil. Adverse pressure gradients cause flow separation because they cause the flow in the boundary layer to be come to a stop in the free stream direction and be ejected from the surface of the airfoil due to continuity. Turbulent boundary layers are able to remain attached through larger adverse pressure gradients because the average flow velocity in the boundary layer (and therefore overall momentum flux) is higher and able to continue moving along the foil surface [1]. The classic example of this is on cylinders or spheres in cross flow as shown in Figure 2.2 which exhibit a significantly lower drag coefficient in the turbulent regime, due to the decreased wake size. In steady state, non-separated flow at the high Reynolds numbers usually associated with flight there is a significant advantage to laminar flow over the wing surface. However turbulent flow allows flow to remain attached on airfoils at higher angles of attack generating higher maximum lift coefficients without the form drag caused by separation. Thus, the ideal situation is a laminar flow airfoil

that is able to remain attached at high angles of attack to mitigate pressure drag, while maintaining low viscous drag due to laminar flow.

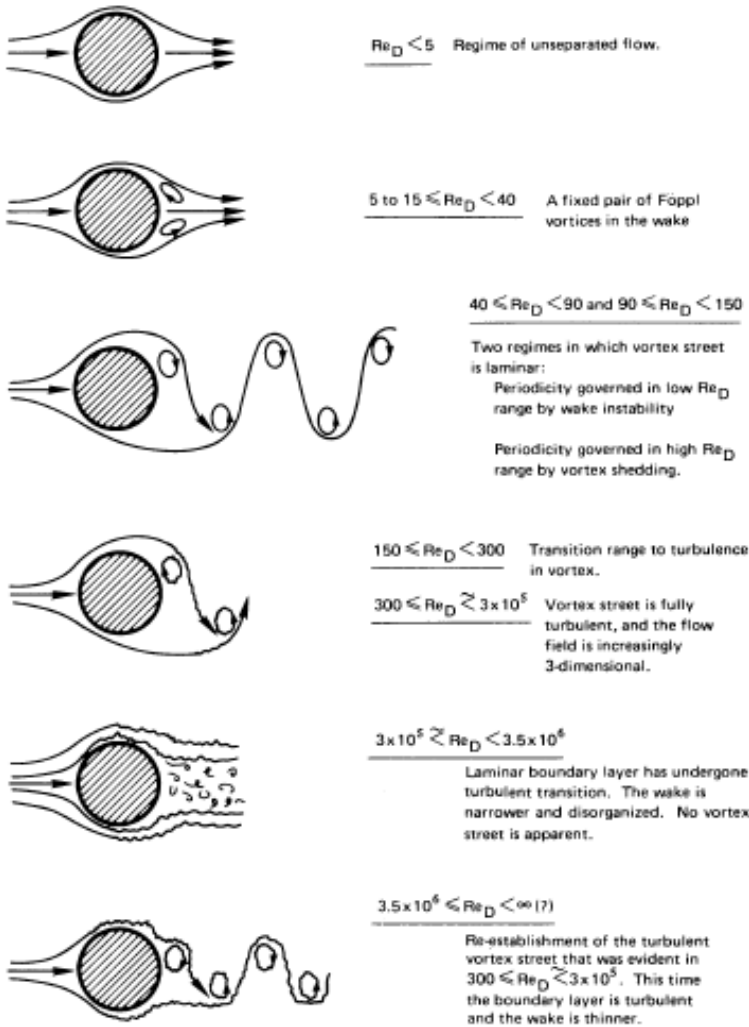


Figure 2.2 Cylinders in cross flow at various Reynolds numbers. Note smaller wake in fifth image with turbulent boundary layer flow than in the third and fourth with medium and high Reynolds number laminar flow [5].

airfoil the maximum thickness point is generally moved aft, and the leading edge of the airfoil is sharper than that of conventional airfoils. Behind the thickest point, after the transition to turbulence and the sudden adverse pressure gradient a concave pressure recovery zone is utilized [7]. Figure 2.3 shows a comparison of various airfoils including conventional and NLF designs. The general design methodology for laminar flow airfoils is to use an inverse design code such

### 2.1.2 Airfoil Design

Natural laminar flow (NLF) airfoils are generally defined as airfoils that are able to maintain laminar boundary layers at least 30 percent along the chord of the airfoil [4]. Laminar flow is maintained by achieving highly favorable pressure gradients in airfoil shape pulling the boundary layer forward and accelerating it over the foil surface so that there is no cause for disturbances that cause the boundary layer to transition to turbulence. In NASA experiments, transition Reynolds numbers as high as  $14 \times 10^6$  were achieved, a significant increase over the usual accepted value of  $5 \times 10^5$  [6]. To achieve favorable pressure gradients further down the chord of the

as the Eppler Design and Analysis code in which a pressure distribution is specified by the user and the program generates an airfoil shape [7], [8]. A laminar flow airfoil design by Honda for a small business jet is shown in Figure 2.4. In this design the pressure gradient is favorable for 42% on the top 63% on the bottom of the airfoil to minimize turbulent boundary layer [7].

Laminar flow is very sensitive to surface roughness and as such very small tolerances are required. Early attempts for laminar flow airfoils on the P-51 mustang and other aircraft in the 1940's and 50's failed due to roughness from the manufacturing processes of the time [4]. At low speed such as during takeoff and landing high airfoil angles of attack are necessary for high lift coefficients. At this point the flow is most likely to separate or transition to turbulence and even slight roughness such as contamination on the leading edge (dirt, bugs or other debris picked up during flight) can cause

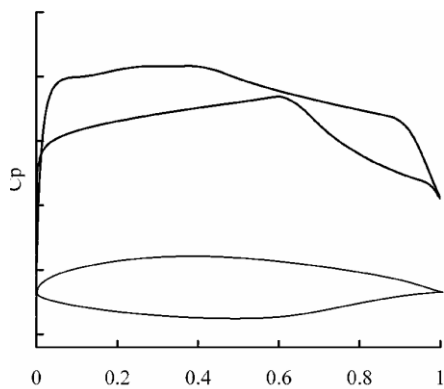


Figure 2.4 Pressure distribution and resulting airfoil for Honda Business jet design. Note favorable pressure gradients followed by concave recovery sections, and their effect on final airfoil shape [7].

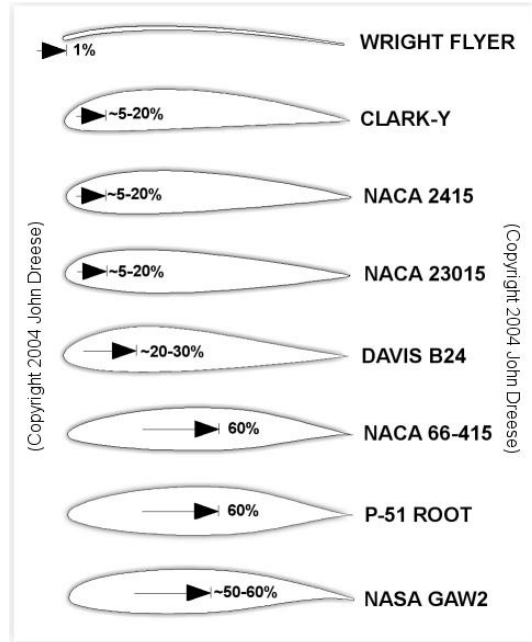


Figure 2.3 Comparison of numerous NLF and standard airfoils and there transition points (NLF transition >30%). Note Laminar flow foils have maximum thickness further aft and a pointer leading edge [7].

stall; resulting in a sudden loss of lift and increase in drag that can lead to a crash. Additionally aircraft control surfaces that allow the pilots to fly the airplane cannot be in the laminar flow region of the airfoil since their increased roughness would cause the flow to transition to turbulence. Most actuators such as ailerons or elevators, used to control the aircrafts roll and pitch respectively, are at the trailing edge of the airfoil so this is not a concern. However slats that extend the leading edge of the airfoil downward to increase camber and lift coefficient during takeoff and landing cannot be used since the increased roughness from their construction

would cause transition to turbulence at the leading edge of the wing even when stowed. Therefore to use NLF airfoils on large aircraft that require slats to produce enough lift for takeoff and landing, technology must be developed that can not only overcome the increased stall potential in laminar flow airfoils, but also allows for high enough attached angles of attack and higher resulting lift coefficients to overcome the need for slats [9].

## 2.2 Flow Control

### 2.2.1 Passive Flow Control

The term *flow control* can be applied to any process in which the flow conditions are changed over the surface of the airfoil. The simplest of these systems are physical adjustments to the airfoil such as the addition of roughness to force transition to turbulence, or physical vortex generators placed on the suction side of the airfoil [10] (Figure 2.5). Vortex generators work by



Figure 2.5 Vortex Generators mounted on the upper surface of a Cardinal II C-177B airplane. They are common on many aspects of commercial aircraft as well including wings, and engine nacelles [11]

creating large streamwise vortices over the wing. These vortices mix high velocity fluid in the free stream with lower velocity fluid at the surface increasing the momentum of the flow in the boundary layer. This allows the flow to overcome large adverse pressure gradients and causes the flow to remain attached at much higher angles of attack

then otherwise possible. In addition to physical vortex generators it has been shown that steady jets of air introduced to the boundary layer before the separation

point generate mixing vortex structures and can be used identically to conventional vortex generators preventing separation [12]. Steady suction of the boundary layer changes the flow state by removing the disturbances that cause the flow to separate [10]. These passive open loop

control systems are often able to produce significant improvements in performance for low complexity and associated cost.

### 2.2.2 Active Flow Control

While passive flow control systems are effective in the lab they are often only effective over a limited range of operating conditions. Outside this range physical vortex generators may increase skin friction, and jets may have no effect or disrupt the flow wasting energy. Active flow control relies on unsteady actuation of the flow, including oscillation within the boundary layer. Additionally active flow control can incorporate closed loop control laws therefore adjusting the flow control techniques depending on the properties observed [10]. A simple version of active flow control is to pulse wall jets with a duty cycle of 10-50%, defined as the time the pulse is active in a given period divided by the total period. In addition to tailoring the amount of control to specific flow conditions, pulsing takes advantage of the transient effects at the beginning and end of the pulse effect to generate large scale turbulent vortex rings which increase the overall mixing effect. Pulsing also requires less overall energy to be added to the flow since the jets are not in constant operation. Yet it achieves the same or more mixing forcing the flow to remain attached [12]. Poisson-Quinton showed in 1948 that separation control is governed by the addition of momentum, and not mass to the flow. As such the parameter that characterizes momentum addition to the flow is  $C_\mu$  the ratio of jet momentum to free stream momentum.

$$C_\mu = \frac{\rho_j U_j^2 j H}{1/2 \rho_\infty U_\infty^2 c} \quad 2.6$$

Where j and infinity refer to the jet and free stream respectively  $\rho$  is the density U is the velocity, H is the characteristic size of the jet (height for a slot, diameter for a jet) and c is the chord of the airfoil[13]. Testing over a fully-separated, deflected flap with steady blowing and periodic excitation at the leading edge of the flap (approximate separation point) showed that with steady blowing  $C_\mu=0.18\%$  was necessary to reattach the flow, and to keep it attached. On the other hand periodic active actuation with  $C_\mu=0.012\%$  was able to reattach the separated flow and  $C_\mu=0.002\%$  was able to maintain attached flow over the flap [14].

In addition to very low duty cycle low  $C_\mu$  pulsing jets, flow control can be achieved without any net mass addition to the flow. Zero net mass actuators add momentum to the flow by oscillating such that there is no external fluid injected into the boundary layer. These systems work by exciting disturbances already present in the boundary layer, accelerating their growth into “large coherent structures.” These structures transfer high momentum fluid to the surface in exactly the same way as the vortices induced by the addition of high momentum jets or pulses. While the structures in the flow themselves as well as the actuation mechanism are unsteady they have a much smaller time scale than the standard vortices usually generated by the airfoil during separation, and therefore act to stabilize the flow[15]. These systems are very simple and do not require plumbing as is necessary for puffer or suction systems. Additionally they have been shown to achieve similar separation control effects with overall momentum coefficient two orders of magnitude lower than those required in steady blowing control situations [14]. To achieve the maximum amount of control with the minimum input momentum the frequency of the forced oscillations should be matched to the frequency of the already present disturbances in the boundary layer [16]. Given a high enough forcing amplitude these disturbances can be manipulated into coherent structures necessary for active oscillatory flow control.

Multiple methods of exciting disturbances in the boundary layer without artificial injection of momentum have been researched with varying success. One of the simplest methods

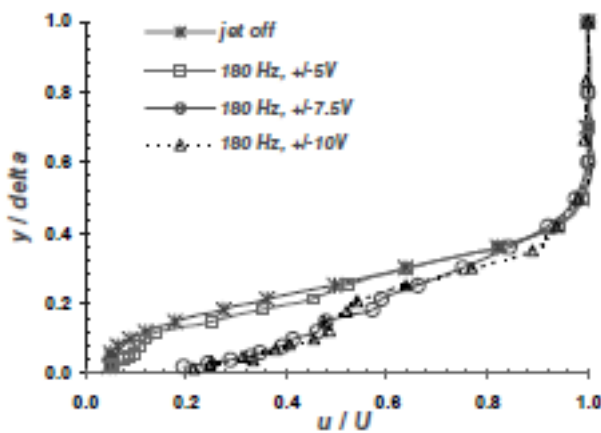


Figure 2.6 Boundary layer velocity profiles using synthetic jet actuators for flow control over an initially stalled portion of an airfoil from Lee et al [16]. Note attached flow above threshold of excitation.

of introducing excitation to the flow is with surface motion, usually in the form of a ribbon or a small oscillating flap that causes momentum transfer at the frequency of the vibration. Another method is acoustic excitation using sound at the frequency of disturbance waves. In general this is tested by placing speakers in the walls of a wind tunnel to affect the entire free stream flow as well as the boundary layer. Using this method disturbances are

generated when acoustic standing waves in the tunnel generate transverse velocity at the airfoil surface. While this method was effective in some select cases it rarely produced a significant increase in the maximum lift coefficient and was only effective across small ranges, similar to many passive flow control techniques. Additionally very large sound levels of over 150 db were required to produce any meaningful changes in flow [14].

One of the most researched methods for zero net mass actuation is the synthetic jet actuator (SJA), a micro-electro-mechanical system (MEMS) device. SJA's consist of a small (less than 1-mm) jet nozzle attached to a cavity with a simple mechanical oscillator which generates jets into and out of the cavity as it vibrates. SJA's can be actuated using piezoelectric material or other simple electric actuators with variable frequencies. When fluid is pushed out of the orifice it generates a vortex ring that is unaffected by the suction as the oscillator returns to its original position. This vortex pulls high velocity fluid into the free stream and therefore generates the necessary momentum to overcome adverse pressure gradient and maintain attached flow. In addition to an ideal excitation frequency there is a threshold of forcing amplitude shown in Figure 2.6. When the correct excitation and frequency are applied to the boundary layer the addition of synthetic jets can have pronounced effect on separation over the entire surface of the airfoil shown in Figure 2.7, also from the research of Lee et al [16].

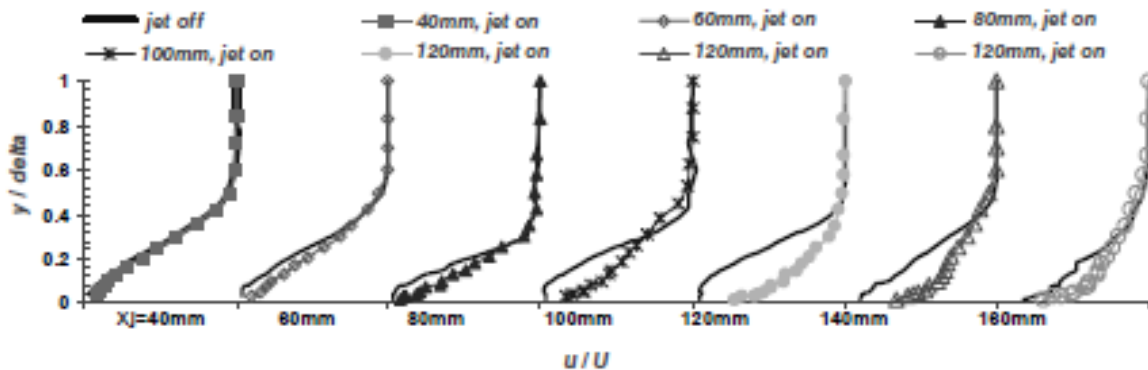


Figure 2.7 Boundary layer velocity profiles at various points over an otherwise stalled airfoil. Note consistent attached flow caused by the synthetic jet [16].

### 3.0 EXPERIMENTAL APPROACH

To test the effect of impinging air jets on laminar airfoil flow a NLF(2)-0415 laminar airfoil was placed in the Tufts 35cm Wind Tunnel, and tested at a stalled angle of attack  $\alpha=8^\circ$  and a chord Reynolds Number based on chord of 27,000. Flow visualization was used to generate high quality images of the flow characteristics. These images were compared to test the effect of the impinging air jets against no flow control and the more standard approach of injecting air along with the free stream. A sheet of smoke was generated directly upstream of the airfoil and still photographs were taken of the smoke. A digital SLR camera and high intensity low duration strobe light were used to take pictures of the smoke so they would not be blurred or distorted. Pulses of air were injected into the boundary layer along the upper (low pressure) side of the airfoil and pictures were taken at various instants after the pulse to determine the effect of the air jet.

#### 3.1 Wind Tunnel

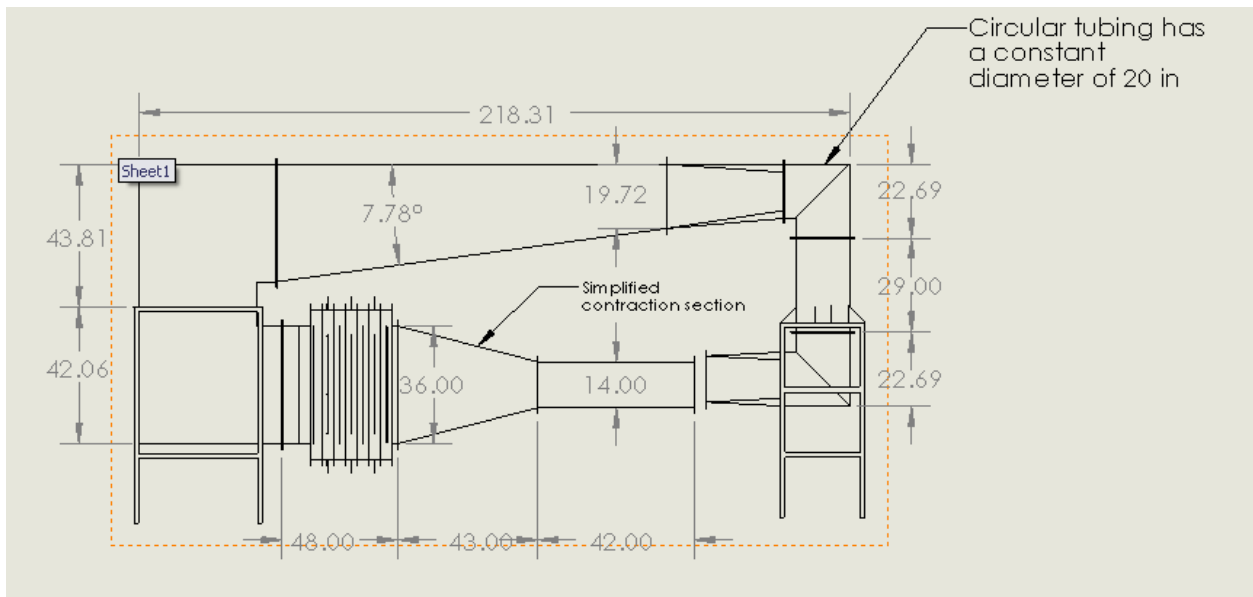


Figure 3.1 Schematic of Wind Tunnel. All dimensions are approximate.

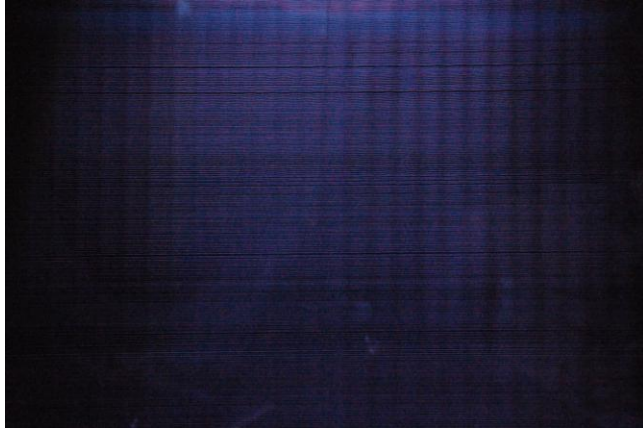


Figure 3.2 Smoke flow in wind tunnel sufficiently far away from walls to avoid wall effects note clean laminar flow.

The Tufts 35-cm Wind Tunnel includes a forty-two inch long fourteen inch square plexiglass test section. A schematic of the tunnel is given in Figure 3.1 in the current setup it is able to achieve velocities up to approximately 18m/s and with simple modifications to the fan blade pitch is capable of over 30m/s. For the purposes of this research the tunnel was operated at 1.5 m/s so that the smoke generated could be easily observed in photographs. Each wall

of the wind tunnel is separated into three separate equal plexiglass sheets such that test components can be easily mounted and removed from the tunnel. At this point no quantitative turbulence intensity data is available on the wind tunnel as turbulence characterization tests have not yet been performed. However visualization of smoke flow through the tunnel as shown in Figure 3.2 confirm straight and clean flow lacking any macroscopically visible turbulence or defects. These tests were performed identically to the flow control tests described in section 3.6.

### 3.2 Airfoil

A NASA/Langley NLF(2)-0415 laminar flow airfoil (Figure 3.3) was selected for experimentation. This airfoil generates lift at all angles of attack ( $\alpha$ ) above -4.0 degrees, separates at -0.5 degrees and generates maximum lift at an angle of 6.0 degrees. A plot of lift coefficient ( $C_L$ ) is shown is given in Figure 3.4. This airfoil is ideal for these tests because the very low stall angle allows us to very easily vary the angle of attack within the stalled regime and experiment with separation mitigation via flow control. Additionally since the airfoil acts very similarly across a large range of Reynolds numbers ( $Re$ ) the tests performed at a necessarily low  $Re$  can be extrapolated across all situations. Full airfoil specifications are included in Appendix A from the Airfoil Investigation Database [3].

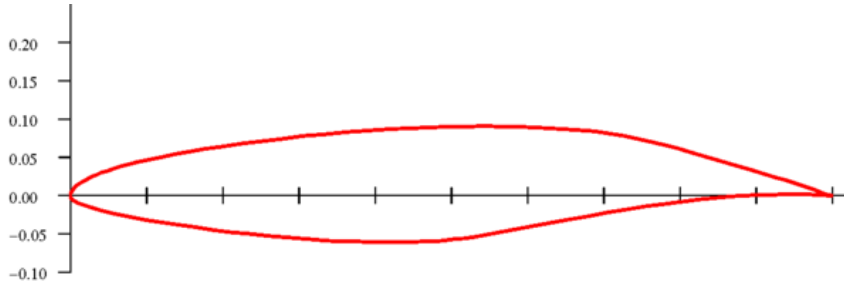


Figure 3.3 NASA/Langley NLF(2)-0415 airfoil [3]

For the purposes of this research an airfoil with a 12in chord was assembled from two pieces built using a STRATASIS 360mc fused deposition molding (FDM) 3D-Printer. The two halves were then glued and bolted together such that threaded rod protruded out of both sides of the airfoil at the  $\frac{1}{4}$  chord point. Using these rods the airfoil could be mounted into the tunnel through holes in the walls, and the angle of attack ( $\alpha$ ) could be adjusted by loosening the bolts and rotating the airfoil in the tunnel. The finish achieved from the FDM machine is very rough due to the machines process of melting and injecting plastic. To achieve a smooth airfoil surface to avoid any roughness effects on the flow, the surface of the airfoil was first filled with a combination of #105 West System® epoxy and #407 Low Density Fairing Filler, then sanded to 600 grit to achieve a smooth fair surface. To fill the final porosity and achieve an

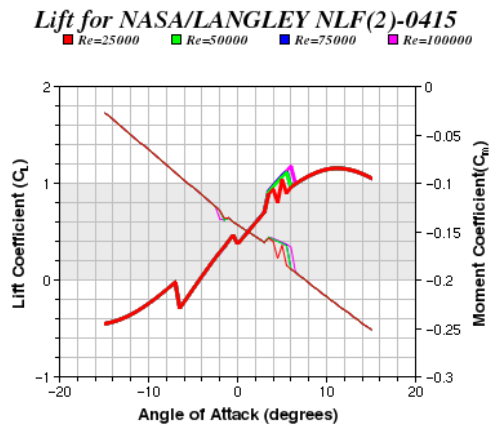


Figure 3.4  $C_L$  and  $C_M$  to angle of attack for the NLF(2)-0415 airfoil, note lift at negative  $\alpha$ , early stall angle and similarity of lift coefficient across a large range of Reynolds numbers. [3]

aerodynamically smooth surface RUST-OLEUM® auto body primer was applied and wet sanded smooth. Lastly RUST-OLEUM® general purpose black semi-gloss automotive paint was applied and wet sanded to 1500 grit until a perfectly smooth and almost reflective surface was achieved. Black paint was chosen so that it reflected the minimum light during the photography. Additionally semi-gloss finish was chosen so that any light reflected would be reflected directly, and not diffused such that there would be the minimum amount of distortion in the final pictures. The finished airfoil is shown in Figure 3.5, technical drawings for the airfoil are included in Appendix B.



Figure 3.5 Test airfoil. Note smooth black surface on airfoil and threaded rods to attach foil to outer walls.

### 3.4 Air Puffer

A fuel injector solenoid was connected to a compressed air tank at 100psi to generate precisely controlled puffs of air and direct them at the airfoil. A National Instruments NI 9401 High-Speed Bidirectional Digital I/O module was used to control the air puffer. Used in conjunction with National Instruments LabVIEW® this system provided a maximum delay of 100ns so that air pulses could be generated with precise timing (see Appendix C for hardware information). The solenoid was then attached to a 3/16" stainless steel tube and finally the tube was attached to a 1-mm stainless steel hypodermic tube bent to direct the flow at the airfoil. This setup is shown in Figures 3.6 and 3.7. The puffer device was attached to the bottom face of the test section with the solenoid and air hoses outside, and the 3/16" tube projecting up to one inch below the lower (high pressure) surface of the airfoil. Different configurations of hypodermic tubing were built to direct a small but powerful pulse at the leading edge of the airfoil. Therefore the only part of the puffer disrupting the flow over the airfoil is that of the 1-mm hypodermic tubing to minimize necessary experimental error.



Figure 3.6 (Left) Puffer system.

Five different puffer configurations were used to compare the effect of different impingement angles and positions along the airfoil surface:

**Configuration 1:** the air pulse is directed with the free stream along the top surface of the airfoil as a control test to compare jet impingement with direct momentum injection. In this case the outlet of the



Figure 3.7 (Right) Puffer configuration 1 in tunnel. Note only hypodermic tubing disrupts flow over the airfoil (left to right flow direction)

hypodermic tubing was aligned exactly with the surface of the airfoil and placed approximately 1-mm above the surface Figure 3.7.

**Configuration 2:** The jet is aligned to impinge directly on the leading edge of the airfoil in the same direction as the free stream from a distance of approximately 1-mm Figure 3.8.

**Configuration 3:** The jet is aligned 2-mm back from the leading edge 1-mm from the surface of the airfoil, at an angle of 45 degrees to the free stream flow. This angle is the minimum that prevents air from the jet from moving forward, against the free-stream flow Figure 3.9.

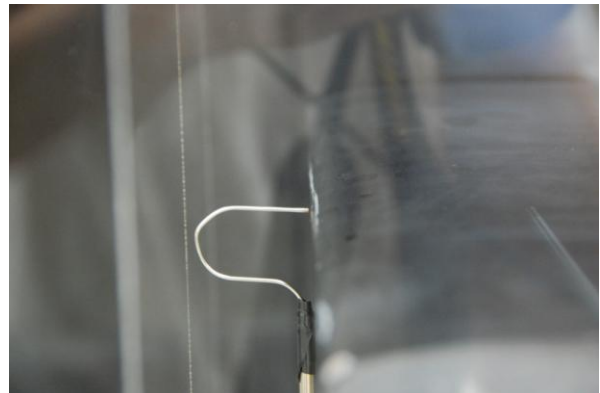


Figure 3.8 Configuration 2 in wind tunnel. Smoke wire in background

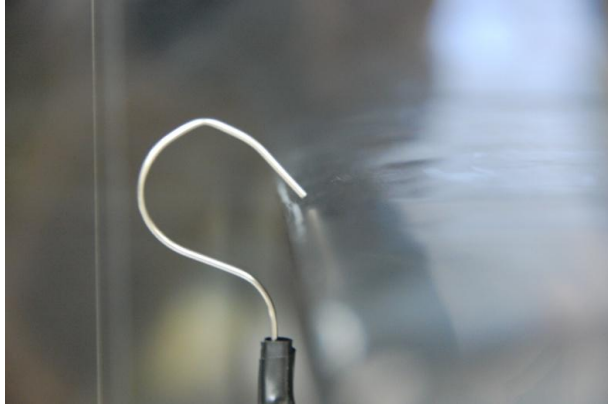


Figure 3.9 (left) Configuration 3

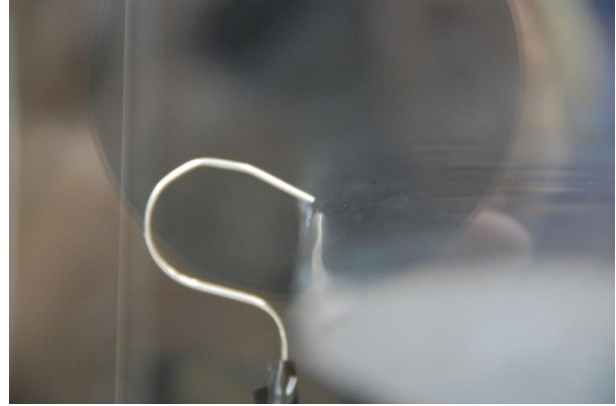


Figure 3.10 (right) Configuration 4

**Configuration 4:** The jet is set up identically to configuration three however the angle is changed to 22.5 degrees above the free stream flow Figure 3.10.

**Configuration 5:** the jet impinges 1.4 inches back from the leading edge and 1-mm above the surface of the airfoil at an angle of 45 degrees Figure 3.11.

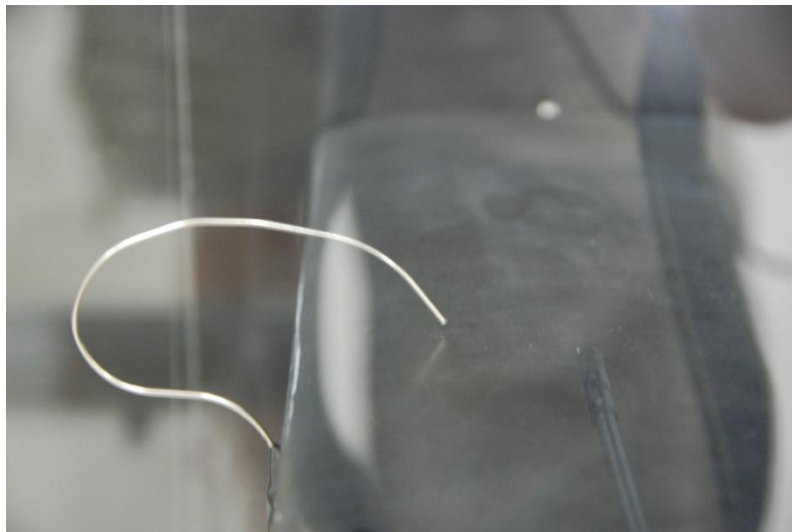


Figure 3.11 Configuration 5

### 3.5 Flow Visualization

A 38 gauge (.00397") Nickel-Chromium (Chromel C) wire was strung vertically across the wind tunnel one inch up-stream of the test airfoil to produce sheets of smoke for flow visualization. This thin wire is necessary to minimize disturbance to the flow that

appears as the Reynolds number based on wire diameter approaches 100 [17]. With a flow speed of 1.5 m/s and standard temperature and pressure (STP) this requires a wire diameter of less than 0.032 inches. However tests performed using a 28 gauge (0.0126") wire as suggested by an undergraduate thesis by David Szarko at MIT showed that large droplets formed on the wire and these droplets produced flow disturbance even at only 1.5 m/s [18] (Figure 3.12). The wire was attached to a variable DC motor controller and a CRYDOM MODC5 relay such that current

could be provided to heat the wire on command. In order to produce smoke the wire was coated before every test with Eliminator Lighting High Quality Fog Juice. This fog juice is water based, and consists of a combination of water and propylene glycol. The mixture of this exact fog juice is unknown, but in general the percentage of propylene glycol is between 10 and 75% depending

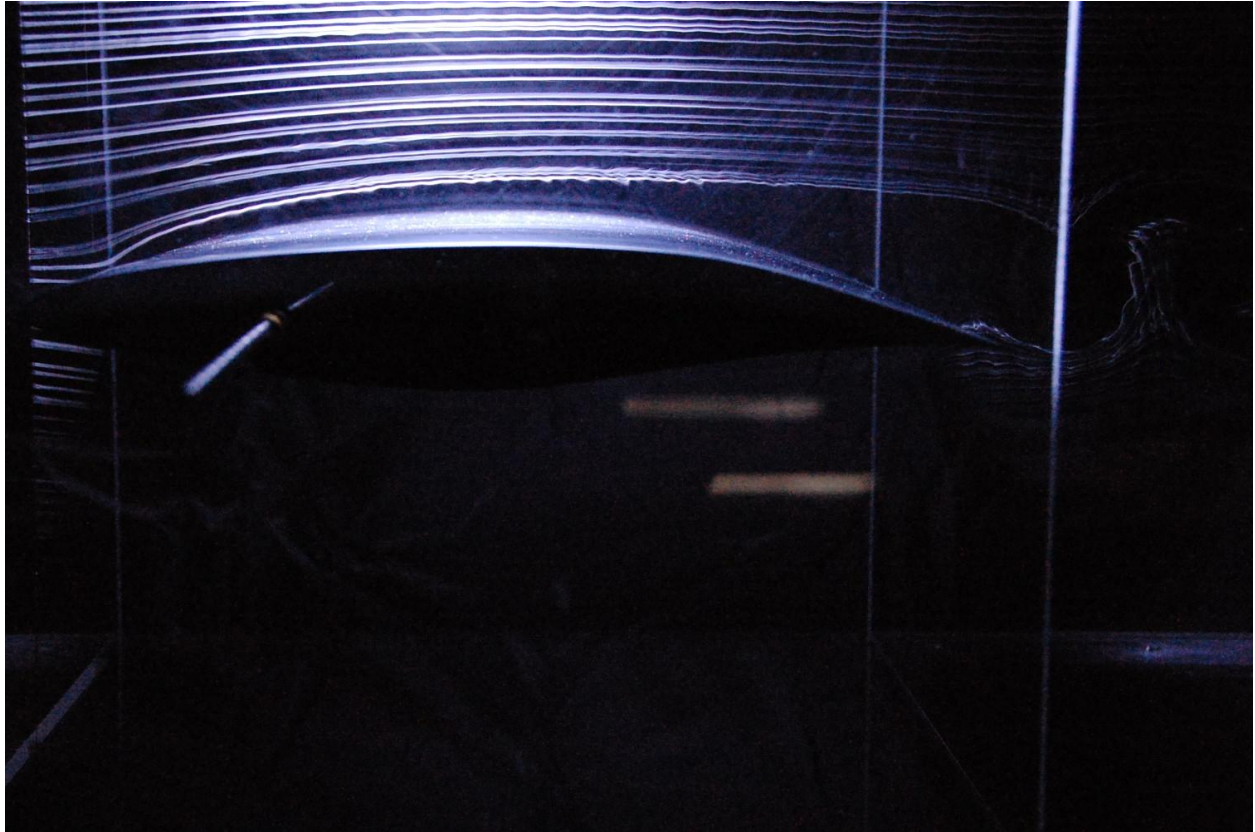


Figure 3.12 Test of smoke produced by 28 gauge ni-chrome wire across a 0 degree airfoil. Note large droplets on the wire and disturbed eddying flow in the streamlines. Compare to Figure 3.2 smoke produced by 38 gauge wire with perfectly smooth clean flow in the wake of the wire.

on the density of fog desired [19]. A length of plastic tubing attached to the smoke wire at the very top of the test section was used to direct a droplet of fog juice to drip down the wire. To apply the fog juice a drop was forced through the tube and allowed to fall down the wire. The surface tension between the wire and the droplet was enough to evenly coat the wire with small droplets of fog juice. However care had to be taken to ensure that the droplets were even and small, otherwise uneven evaporation of the liquid from the wire produced varying smoke densities in the photograph. A 100 gram mass was attached to the bottom of the wire to keep it straight in the flow and to account for the increase in length due to a change in temperature.

Figure 3.13 shows a schematic of the smoke wire setup and Figure 3.14 shows the plastic tubing used to inject fog juice into the tunnel.

A Nikon® D40 digital SLR camera (Appendix C), with a Nikon® AFS NIKKOR® 18-200-mm manual or automatic focus lens was used to take pictures of the flow. The camera was set up in a computer controlled mode using Nikon’s Camera Control Pro® software. The camera was placed 18 inches from the side panel of the wind tunnel and about 25 inches from the smoke

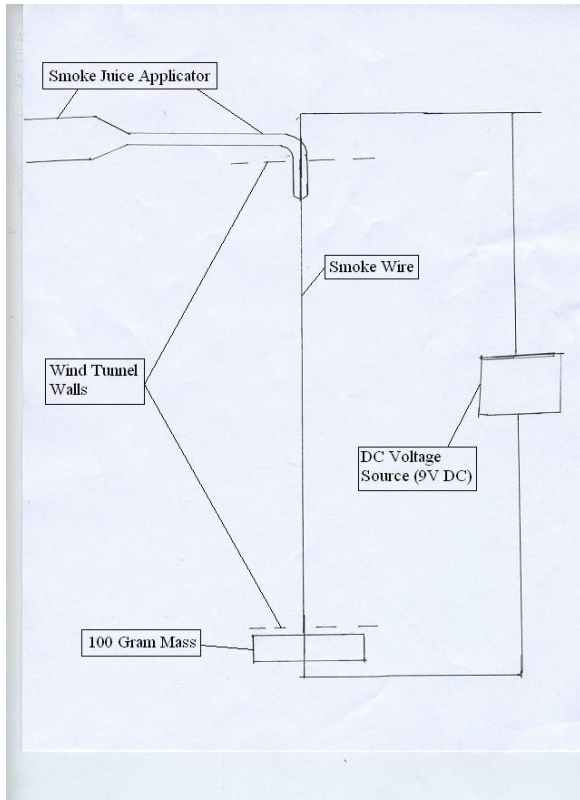


Figure 3.13 Schematic drawing of smoke wire setup.

Therefore in order to generate no smearing and enough light to easily see the smoke the pictures were taken using an open shutter and a high speed strobe light in a completely dark room.

The strobe light used is a custom built SPOT flash system from Prism Science Works (Appendix C). This system generates a peak intensity of 69 million lumens with a flash duration of less than 500ns[21]. The SPOT system was triggered directly through the NI 9401 to give a less than 100ns margin of error on the flash time. In order to illuminate the smoke and the airfoil perfectly the spot was suspended 1 ft above the upper surface of the wind tunnel test section and

position, pointed at the back third of the airfoil. The aperture size was set to 5.6 to get a picture focused primarily on the sheet of smoke but with some room for error in the focusing of the camera precisely on the location of the smoke. The standard flash speed used with the built in Nikon camera is not nearly fast enough to capture the flow without some distortion due to the movement of the smoke during the flash time. Additionally a standard flash lamp does not produce nearly enough light to illuminate the smoke sufficiently to achieve high quality images. Even Nikons highest quality speed light, the SB-900AF Speed Light®, has a minimum flash time of 1/38,500s or approximately 26ms, and this speed is only achievable at 1/128<sup>th</sup> of the full output, while a 1,136ms flash is necessary for

the edges of the top panels were blacked out such that a 3 inch deep (perpendicular to the flow) column of light entered the test section providing approximately 12" (in the direction of the

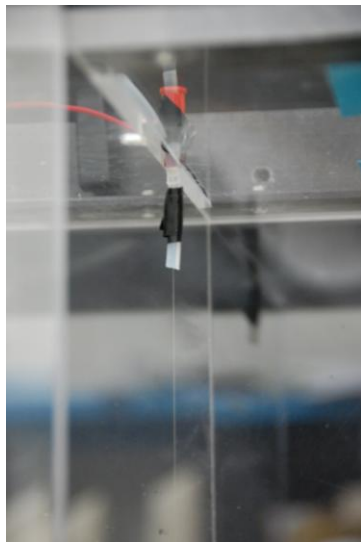


Figure 3.14 Smoke wire and fog juice tubing from inside tunnel. Tube protrudes approximately 1.5" into tunnel.

flow) of good illumination at the airfoil surface. An image of the final strobe setup on the tunnel is shown in Figure 3.15.

Three sources of disturbance in the picture were generated by this experimental setup: the first is flow disturbance at the very top of the wind tunnel, far away from the airfoil surface caused by the tube to inject fog juice onto the wire in the tunnel (Figure 3.14). This flow disturbance is negligible in the flow measurements because it is so far away from the airfoil as to have no effect on the flow, or the pictures. Second are wake vortices generated by the 3/16" tube used to inject the compressed air to the puffer (Figure

3.16). While this flow disturbance is visible on the lower surface of the airfoil and slightly disrupts the flow over

the high pressure side of the airfoil, it has no visible effect on the low pressure upper side of the airfoil where stall occurs and where this research is focused. Lastly visible in all smoke images including Figures 3.2 and 3.16 is the consistent periodic wave in the smoke streamlines, visible as vertical lines of varying smoke density. This is 60Hz vibration in the wire generated by an imperfect DC signal generated by the motor controller that still has remnants of the 60Hz AC signal from the electric grid.

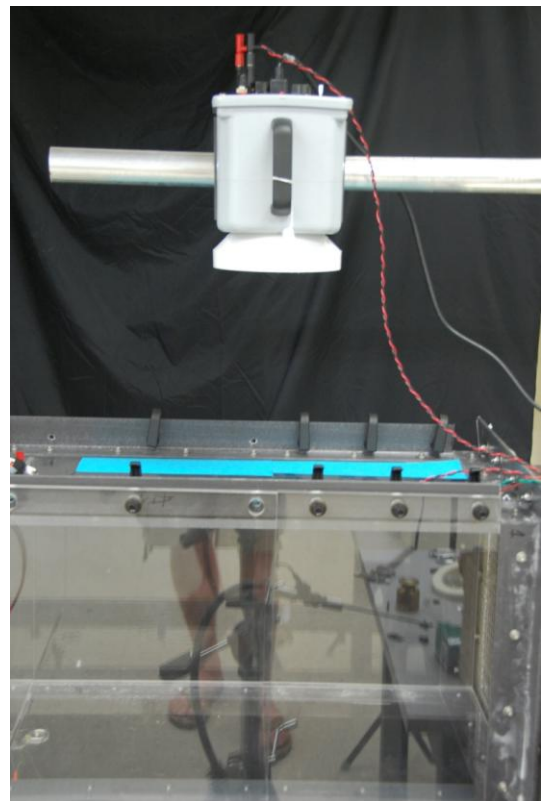


Figure 3.15 SPOT strobe light setup ~12" above tunnel surface.

### 3.6 Test Methodology

A repeatable experimental methodology was generated to make quantitative and qualitative comparisons between flow control tests. Using the systems described in the rest of section three

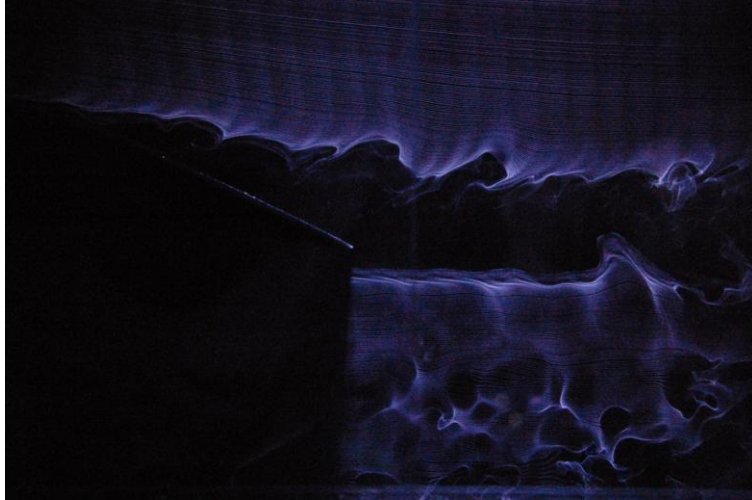


Figure 3.16 Flow over 8 degree NLF(2)-0415 airfoil with no air puffer flow control. Note disturbances below airfoil caused by upstream tubing that do not enter in clean flow above airfoil. Also note clearly visible 60Hz signal in clean upper flow generated by imperfect DC current.

a National Instruments LabVIEW® virtual instrument was created to control the timing off all aspects of the test. Early experimentation determined that the ideal smoke characteristics were generated using approximately 9 volts through the smoke wire and taking pictures between 600 and 1000 ms after the voltage was first applied to the wire, thus all pictures were taken 800ms after the application of voltage. Constant voltage was applied for 5 seconds to completely burn the smoke off the wire during every test.

The smoke wire was placed 1.5 inches upstream of the leading edge of the airfoil, so the flow, and therefore the smoke, would be able to conform back to undisturbed flow before reaching the airfoil.

All tests were performed to demonstrate the effect of one short (5-30ms) pulse and the effect on the flow as the pulse passed over the separated region on the airfoil. The smoke wire was place one inch down the span away from the puffer location to minimize any disturbance in

the flow over the suction side of the airfoil from the tubing required for the puffer system. Images were taken at 50ms intervals from 600 to 800ms after the beginning of the impinging jet pulse and at 10ms intervals between 600ms to the delay necessary such that the jet pulse

Table 3.1 Experiments completed (marked with x)

	Pulse Duration	5ms	10ms	20ms	30ms
Puffer Configuration					
1		X	X		
2			X	X	
3			X	X	
4			X	X	X
5			X	X	X

had not yet reached the separated portion of the airfoil. This provided approximately 54 shots per

experiment representing a complete time history of the flow conditions. After each image was taken it was immediately checked to be certain of good smoke and illumination in the entire flow regime, any images that did not appear to have good data were re-taken. A control image with the air puffer off was taken before every test run so that direct comparisons could be made between each method, and standard flow. Table 3.1 shows each experimental run that was performed.

### 3.7 Analysis Methodology

Smoke wire flow visualization is well suited to first order qualitative comparisons of flow conditions over simple airfoils. It is easy to determine if and where the flow separates from careful scrutiny of the pictures. The comparative size of the separation bubble and any re-attachment effect also can be seen in the images. Additionally it is very simple to determine the location of the flow disturbance caused by the controlling air jets. Lastly vortices shed by the airfoil can be seen in the wake; large vortices appear in the wake of the airfoil, and smaller ones show up as irregularity in the edges of the streamlines outside the wake. Also the direction of the flow behind the airfoil can be determined by analyzing the direction of the stream lines and the wake behind the airfoil.

Quantitative flow visualization techniques were applied to the pictures to get data from the tests. NI LabVIEW® image processing software developed by Tufts University Professor Chris Rogers was used to measure the size of the wake generated by the airfoil under different conditions. The wake width was measured as the distance between smoke streamlines and time averaged across the region on interest in the wake. Major outliers were removed from the data set, such that abnormally large or small values generated by large-scale vortices or computational error did not affect the overall measurement of the wake. As discussed in section 2.1.1 the pressure drag force scales directly with the size of the wake. Therefore to a first order approximation the drag can be estimated by assuming the flow speed in the wake averages to zero and therefore the form drag on the airfoil (per span) can be calculated as the dynamic head times the height of the wake

$$\frac{1}{2}\rho u^2 * h \quad 3.1$$

Where  $\rho$  is the density of the fluid,  $u$  is the velocity and  $h$  is the height of the wake.

## 4.0 RESULTS

### 4.1 Qualitative Comparison

#### 4.1.1 Base Airfoil (No Control)

Flow separates over the NLF(2)-0415 at 8 degrees angle of attack at approximately 2/3 the total chord of the airfoil as seen in Figure 4.1. This image as well as Figure 3.17 in the previous

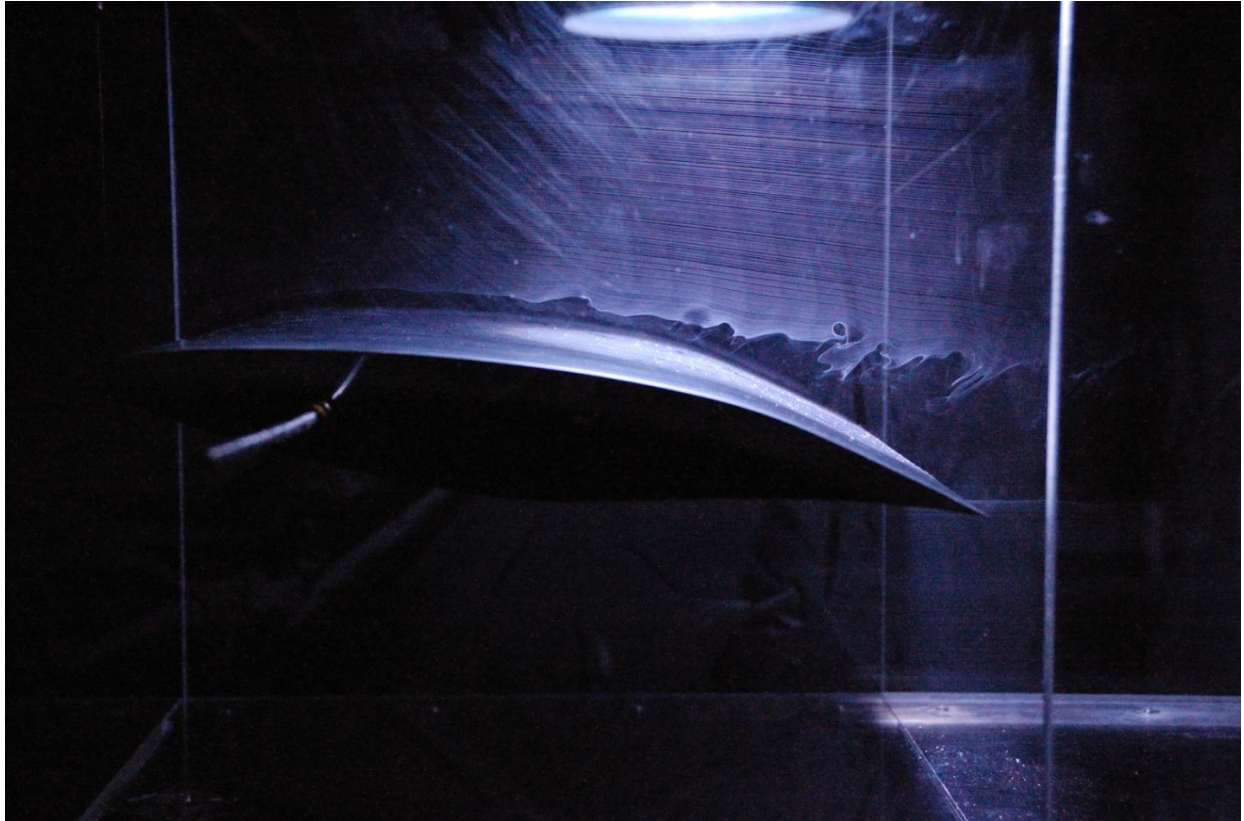


Figure 4.1 Smoke flow visualization over the NLF(2)-0415 airfoil at  $\alpha=8$  with no flow control. Note clear separation at approximately  $x=2/3c$ . A focus on the separated region can be seen in Figure 3.17.

section will serve as the base comparison for all flow control experiments described in this section. In both of these images the wake moves straight behind the airfoil indicating that there is very little circulation added to the flow by the airfoil. In Figure 3.17 it is clear that the separated flow follows the airfoil until about the  $3/4$  chord point when the smoke streamlines begin to go straight with the free stream. This shows that that the last  $1/4$  of the airfoil with the most camber is not providing any lift to the airfoil. No circulation in the flow behind the airfoil demonstrates that at this high, stalled, angle of attack the airfoil is producing very little efficient aerodynamic lift, and is acting similar to a bluff body being pushed along by the flow stream, not

a lifting aerodynamic surface. This result agrees with the data calculated for an NLF(2)-0415 airfoil at  $Re=25000$  shown in Figure 3.4 from the drag polars also calculated at the airfoil investigation database the drag coefficient ( $C_D$ ) at this point is  $C_D=.06415$  [3.2]. A  $C_L/C_D$  chart is included in Figure 4.2 showing that at this drag coefficient the airfoil is far beyond its optimal operating condition generating very high drag with very little increase in lift. In Figure 4.1 it appears that large scale disturbances that eventually help to cause separation appear slightly after the  $\frac{1}{2}$  chord point. After separation these disturbances generate high frequency eddies apparent in the suction side of the wake visible in Figure 3.17. (Flow disturbance visible below the surface of the airfoil cannot be analyzed as some if not all was caused by the puffer setup described in

section 3.4; also the flow below Figure 4.1 without the puffer shows clean wake flow below the bottom surface).

**Drag Polar for NASA/LANGLEY NLF(2)-0415**

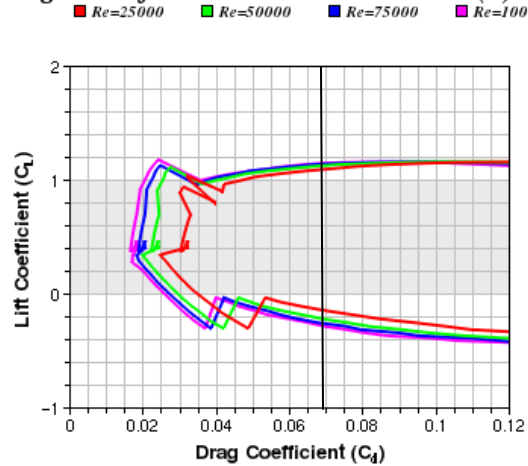


Figure 4.2 Drag polar for NLF(2)-0415 airfoil. Black line at  $\alpha=8$  operating condition ( $Re=25000$ ). Far beyond ideal operating condition with very high drag conditions [3]

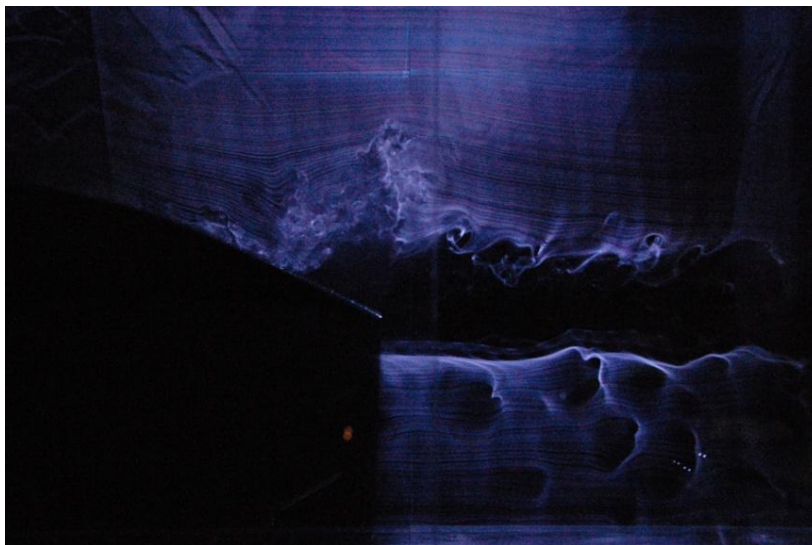


Figure 4.3 Fully attached flow over 3/4 of the usually separated region generated with a 10ms streamwise pulse

#### 4.1.2 Streamwise air jets

We investigated 5 and 10ms 1-mm streamwise air jets (Configuration 1) to test the effect of streamwise jets for flow control, so direct comparison could be made to the effect of impinging jets. 5 and 10ms pulses had some attachment effect immediately after the pulse passed the separated portion of the airfoil.

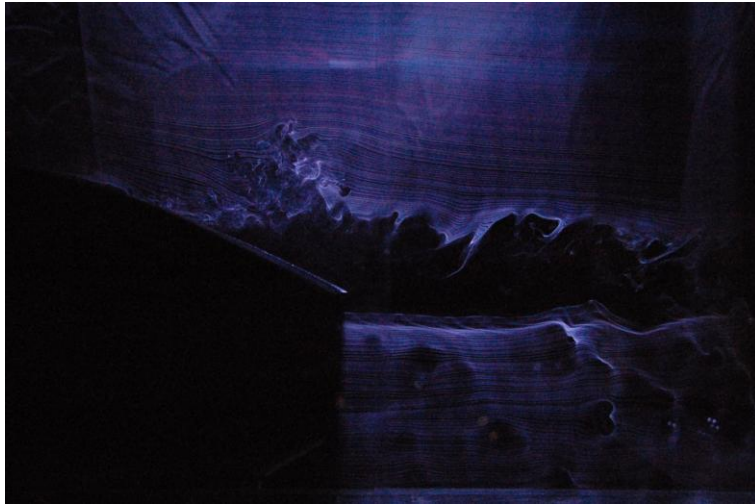


Figure 4.4 Fully attached flow over  $\frac{1}{2}$  of the usually separated region generated with a 5ms streamwise pulse

The ten ms pulse (Figure 4.3) is able to attach 75% of the separated region and the 5ms pulse (figure 4.4) 50%. Additionally the 10ms pulse causes the flow to completely re-attach to the trailing edge immediately after the pulse passes, but as shown in Figure 4.5 a small separation bubble appears at the initial separation point. For both pulse durations some time after the pulse passed circulation was

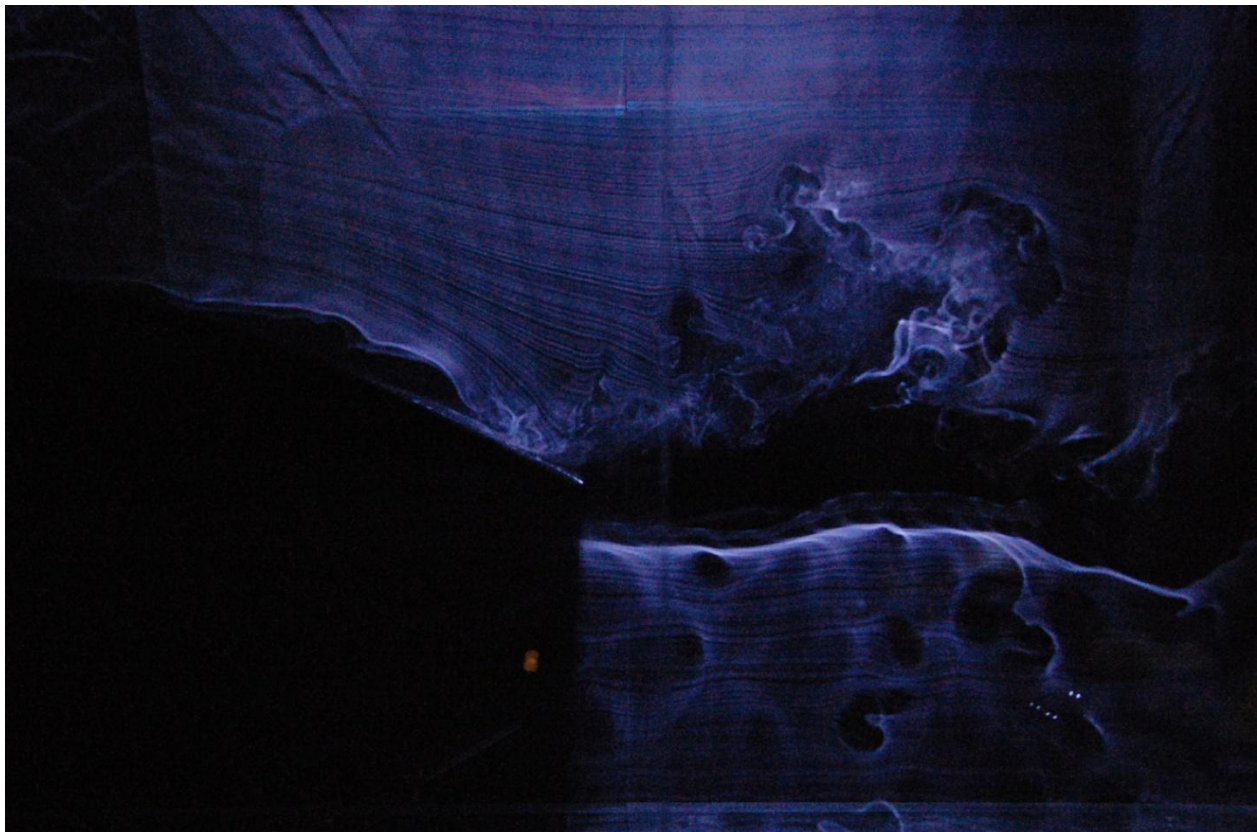


Figure 4.5 Flow as 10ms pulse passes trailing edge of airfoil not attached flow at trailing edge following the pulse, but separation bubble starting at initial separation point.

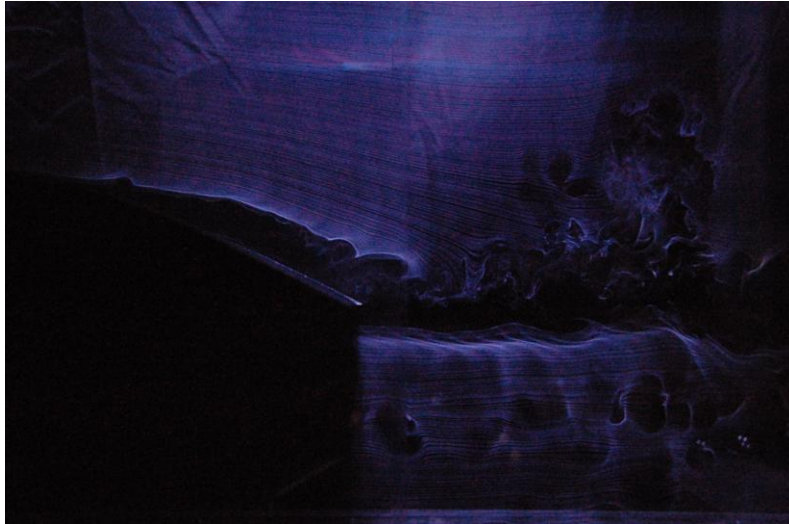


Figure 4.6 Flow conditions 40ms after 5ms pulse passed the trailing edge. Note separated flow that still is affected by shape of the airfoil and circulates around the general shape causing lift.

maintained in the flow. Although the flow was separated from the airfoil it followed the contour indicating a likely increase in lift and a decrease in form drag shown in Figure 4.6. Both the 5 and 10ms pulse maintain additional circulation around the airfoil, decaying until approximately 200ms after the pulse passed the leading edge, when the circulation effect disappeared. At this point

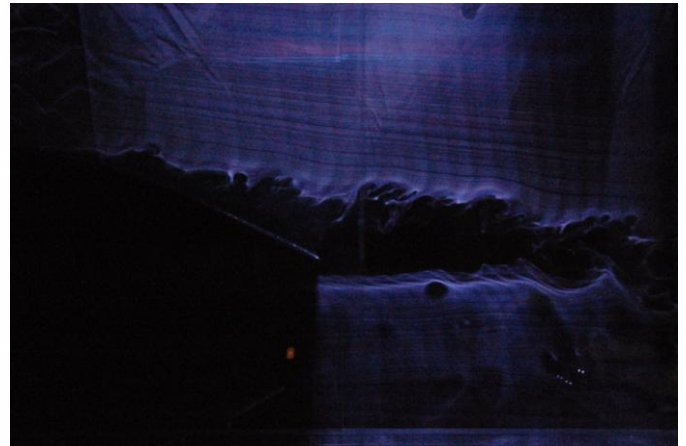
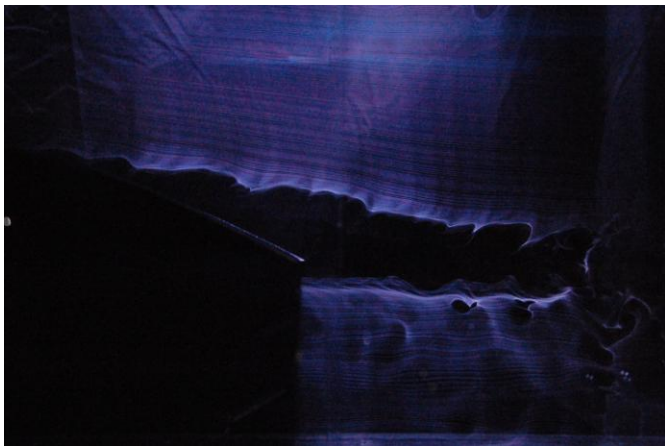


Figure 4.7 Flow 250ms after the 5ms streamwise pulse passes the trailing edge of the airfoil. Note very clean edges of the smoke indicating the lack of small scale vortices clear in un-controlled flow. Figure 4.8 Flow 450 ms after 10ms streamwise pulse note return to rough flow edges near airfoil and large scale vortices generated near right edge of picture.

the size of the wake was still qualitatively smaller suggesting that at this point there was no appreciable increase in lift, but some decrease in drag was still apparent. This decrease in wake size was maintained for both conditions for another 150ms until the wake size was approximately the same as the tests without an initial air jet. Additionally as can be seen in Figure 4.7 taken 250ms after the 5ms pulse passed the leading edge, the wake while the same size as that of the zero flow control case has much fewer and smaller high frequency

disturbances. This effect appears in the 10ms pulse tests as well and lasts 350ms after the pulse passes the trailing edge. In the larger duration pulse 450ms after the pulse passes the trailing edge large scale eddies are produced behind the airfoil, as it transitions back to flow identical to the original flow generated without control (Figure 4.8). In the 5ms pulse this effect does not appear but instead the flow transitions sharply back to the original conditions with clear small fluctuations 350ms after the pulse passed the trailing edge.

### 4.1.3 Leading Edge Impingement

The first configuration of impinging jets tested for flow control were 1-mm jets directed straight at the leading edge of the airfoil (configuration 2) for durations of 10 and 20ms. Unlike the streamwise jets there was a significant difference in the flow characteristics between the 10 and 20ms jet. While the large scale disturbance directly caused by the pulse is visible in the 10ms pulse (Figure 4.9) there is no significant effect on flow attachment. Additionally later images with the pulse further past the trailing edge show no significant decrease in wake size behind the airfoil. In fact the only noticeable difference in the flow after the pulse has passed is the lack of irregularity in the flow after the pulse has passed. This

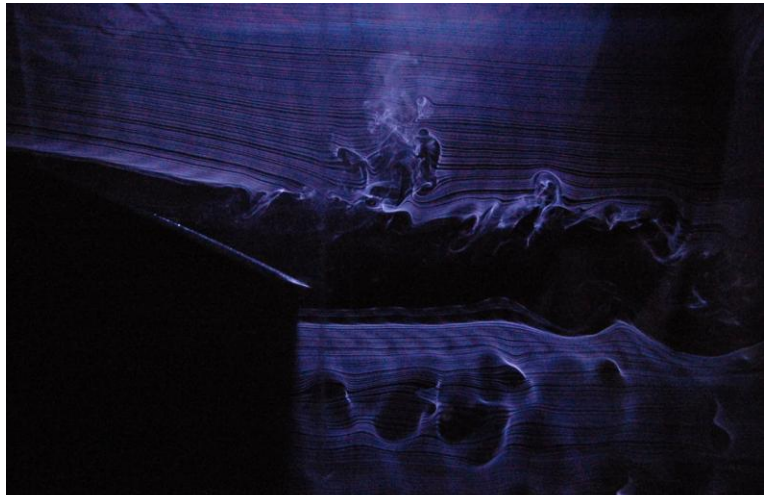


Figure 4.9 10ms impinging pulse directly at leading edge. Note disturbance caused by pulse past trailing edge of airfoil, but no increase in attachment or circulation around the airfoil.



Figure 4.10 20ms leading edge impinging jet able to cause the flow to reattach over about 50% of the initially stalled region of the airfoil.

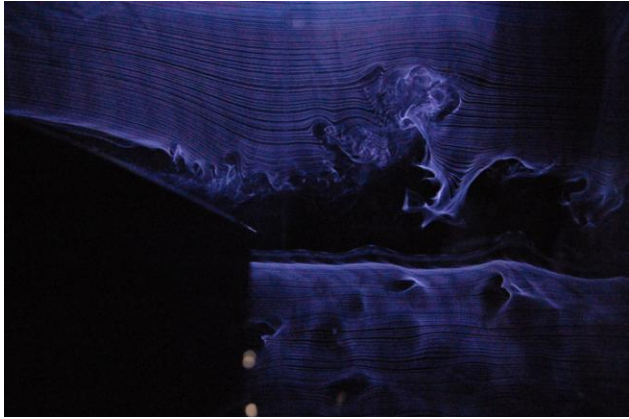


Figure 4.11 As the 10ms pulse passes the trailing edge it generates a significant change in the overall shape of the flow and increases circulation, but is unable to reattach the flow to the trailing edge of the airfoil.

(Figure 4.11). After the pulse passes the trailing edge it is able to maintain both the circulation and the decrease in wake size for about 170ms, with slight loss of effect over time. However by 200ms after the pulse has passed the effect is suddenly almost completely gone and the flow conditions return to their initial stage except for the roughness in the edges that begins to reappear at this point. The disturbance in the flow generated by the jet pulse is also visibly different for the impinging air jet. In the case of the 20ms pulse, the vortex generated by the

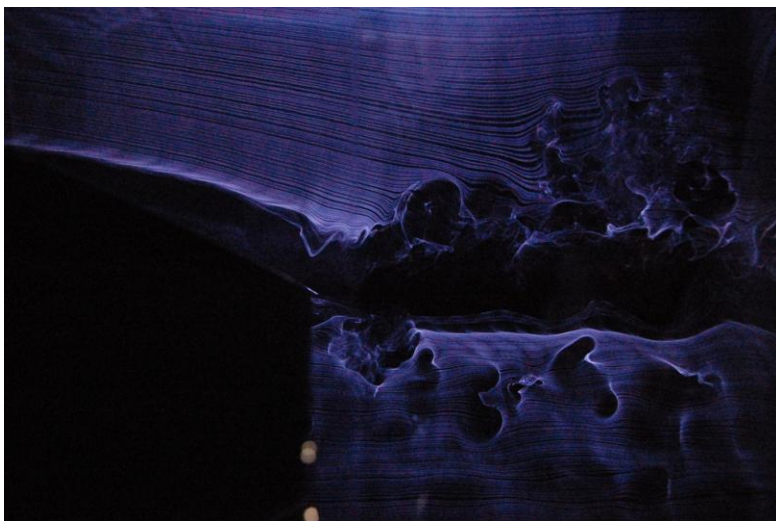


Figure 4.12 20ms impinging pulse after it has passed the trailing edge. The structure directly generated by the pulse is spread out and undefined as compared to the vortex generated by the tangential stream jet that appears to generate a much more coherent structural shape seen

effect lasts 300 ms after the pulse passes the trailing edge of the airfoil.

Unlike the 10ms pulse the 20ms pulse is able to generate increased attached flow as well as circulation around the airfoil and decrease wake size. Similar to the 5ms tangential puff in section 4.1.2 the 20ms impinging jet is able to force the flow to attach over approximately the first half of the stalled region (Figure 4.10). The pulse however is not able to get the flow to reattach at the trailing edge unlike the tangential jet

pulse is much less coherent and much more spread out in the stream wise direction, as shown in Figure 4.12. As seen in Figure 4.9 the structure generated by the 5ms impinging pulse is also very indistinct, though much smaller and less spread out the smoke is still mixed in with the dark areas in the vortex as opposed to the disturbance generated by the tangential pulse in Figures 4.4-4.6 which appear much more distinct

for both pulse durations. 225ms after the pulse passes the trailing edge, the wake begins to show large scale vortices which remain until 325ms after the pulse (Figure 4.13). After these large scale eddies disappear the flow returns to its original condition with small disturbances appearing in the smoke at the edges of the wake.



Figure 4.13 Large scale vortices appear in the wake between 225 and 325ms after the configuration 2 pulse passes the airfoil. This image is taken 300ms after the pulse, note wake edges still well defined.



Figure 4.14 10 ms configuration 3 pulse generated in configuration three passing over the airfoil. Note very little effect on attachment or wake size. Additionally note small vertical disturbances in flow stream that appear fairly unstructured.

#### 4.1.4 45-degree Impinging Jets Above the Leading Edge

Similar to the 10ms jet pointed directly at the leading edge a 10ms jet pointed at the top edge of the airfoil just aft of the leading edge at 45 degrees (configuration 3) has very little effect on the separation of the flow. Once

again the pulse was able to smooth the edges of the flow in the wake, but was unable to produce meaningful effect in separation or in overall wake size. The disturbance shape in the 10ms impinging jet is similar to the 10ms direct leading edge jet shown in Figure 4.9. The 45 degree case (Figure 4.14) generates two distinct disturbances that, similar to the one in Figure 4.9, seem to go vertically into the free stream, but are very thin and have very little coherent structure. In other images these

disturbances morph somewhat into different shapes, further demonstrating that the disturbance shape is irregular. Significantly after the air pulse passed the airfoil surface (130ms after the trailing edge) the wake

began to undergo large scale oscillations shown in Figure 4.15. These oscillations formed a large wave pattern in the wake of the airfoil with a wavelength of approximately the length of the

airfoil and moved the wake perpendicular to the stream approximately  $1/8^{\text{th}}$  to  $1/4$  of the total height of the wake.

The 20ms configuration 3 pulse generates three distinct modes of flow control. The first

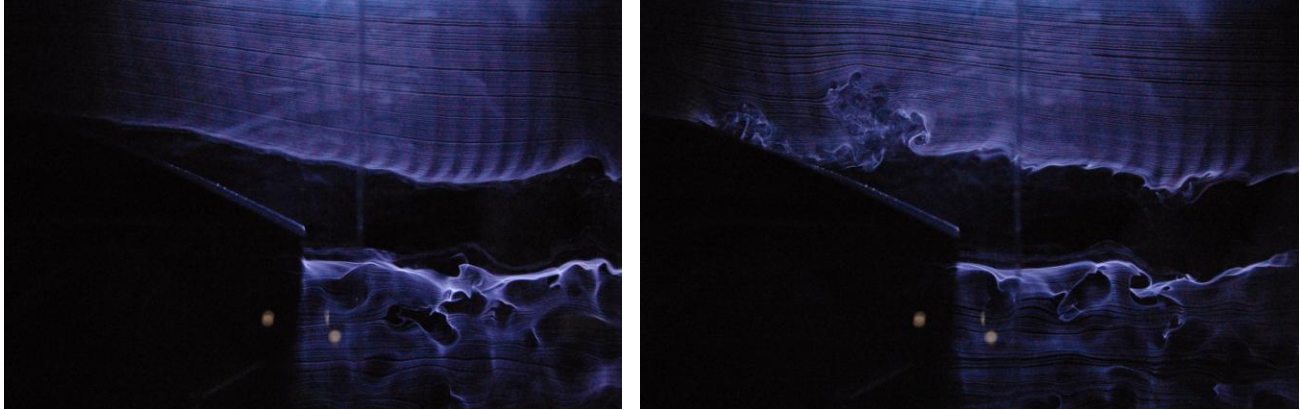


Figure 4.15 (left) Flow 130ms after the 10ms pulse passed the airfoil. Note wavelike shape of the wake curving behind the airfoil then returning with about half the wavelength occurring in the frame of the image.

Figure 4.16 (right) Flow as the 20ms pulse passes over the airfoil note attached flow between two distinct vortices. These vortices become vertical and much more defined as they progress further along the airfoil.

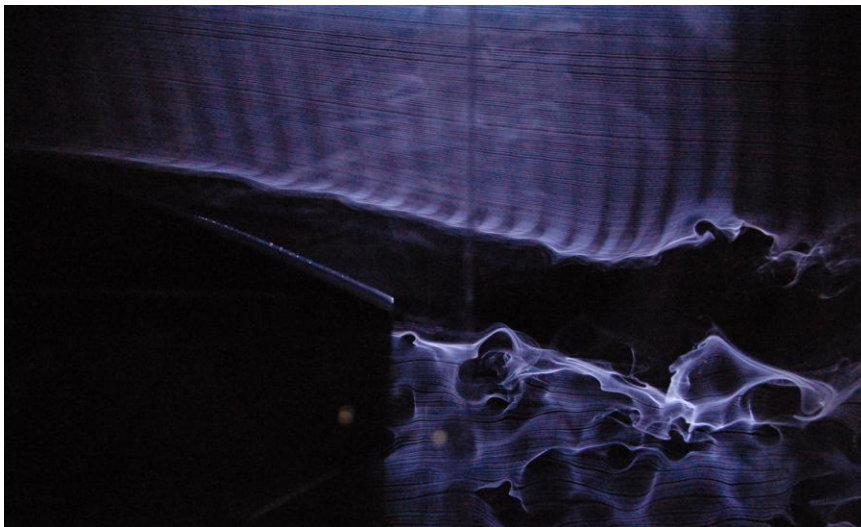


Figure 4.17 Flow conditions 120ms after the 20ms pulse has passed the airfoil. Circulating vortices begin to appear in the flow eventually leading to a smaller wake and increased flow circulation around the airfoil shown in figure 4.18

of these modes is as the pulse passes over the separated region on the airfoil. Similar to the 10ms pulse the 20ms pulse generates two distinct vertical structures in the flow. They are significantly more separated in the 20ms pulse suggesting that they are generated when the pulse begins and ends. As shown in Figure 4.16 the flow is able to remain attached

between the two vortices and to some degree after the second vortex for approximately 50% of the usually separated region. After the puff passes the trailing edge of the airfoil, there is very

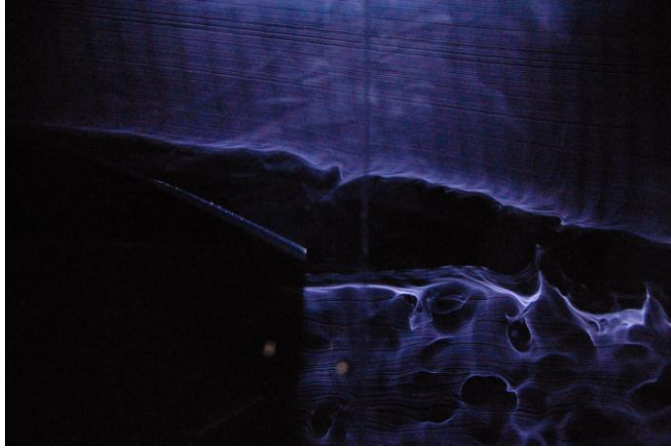


Figure 4.18 Flow conditions 250ms after the pulse has passed the trailing edge. Note increased rotation around the airfoil as well as smaller wake conditions.

little effect on the flow conditions. As usual the boundaries are smoothed, and there is somewhat more curvature along the surface of the airfoil, however there is almost no effect on the overall wake size or shape (Figure 4.17). These flow conditions remain until about 120ms after the pulse passes the airfoil when large vortices begin to appear in the wake. These vortices continue to be produced, decreasing in magnitude for 140ms,



Figure 4.19 Large scale wake vortices that appear 260ms after the pulse and continue until the flow returns to its natural state 240ms later.

during which time the wake shrinks and moves downward showing increased circulation around the airfoil (increased lift), and decreased drag during period time as can be seen in Figure 4.18.

After this point (260 ms after the pulse) very large vortices begin to appear (Figure 4.19) and the wake appears to be a similar size and shape to the un-controlled flow until 500ms after the pulse when the flow conditions return to the conditions without the pulse, showing roughness at the boundaries and completely separated flow over the trailing edge of the wing.

#### 4.1.5 22.5-degree Impinging Jets Above the Leading Edge

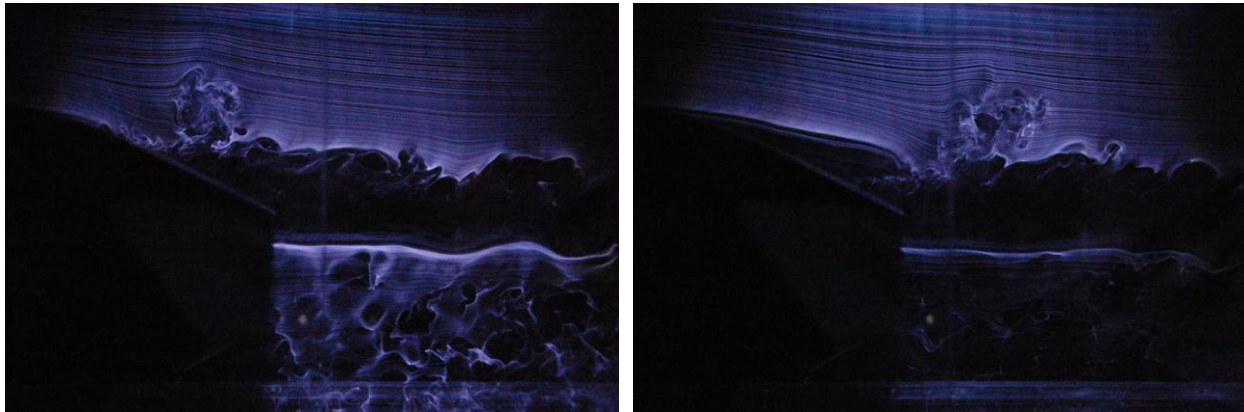


Figure 4.20 (left) 10ms pulse generated using configuration 4. Note attached flow behind the pulse covering approximately 50% of the usually separated area.

Figure 4.21 (right) Flow conditions as 10ms pulse at 22.5 degrees passes the airfoil note flow curving down distinctly at the trailing edge right upstream of the pulse vortex.

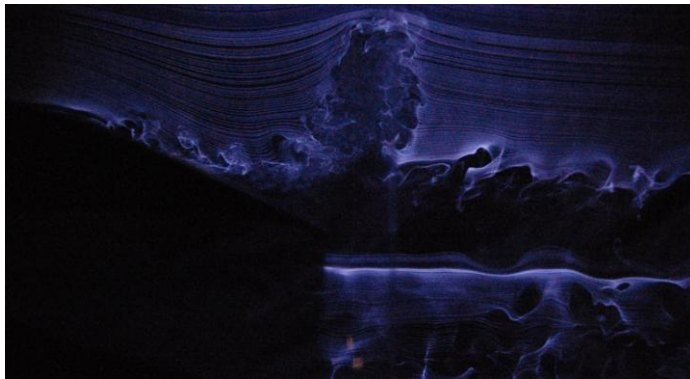


Figure 4.22 75% attached flow generated by a 30ms pulse from at 22.5 degrees (configuration

Qualitatively the flow conditions are very similar between the 20ms impinging jet at 45 degrees discussed above and the 10ms pulse generated 22.5 degrees above the freestream as produced by configuration 4. As the puff first passes the airfoil it is able to maintain attached flow over the first 50% of the airfoil (Figure 4.20). Additionally as the flow passes the trailing edge of the airfoil it causes the

flow stream to curve along with the foil initially Figure 4.21 (an effect not seen in the 20ms pulse from configuration 3) and then to curve slightly along with the trailing edge of the foil, then progress straight off the back. This generates similar wake size and shape to that generated by

the 20ms, 45 degree pulse shown in Figure 4.17. 100ms after the pulse passes the airfoil vortices are generated of a slightly smaller magnitude than in the previous tests, and a smaller wake that follows the shape of the trailing edge more closely is visible. Lastly 240ms after the pulse passes even larger vortices appear and the flow conditions gradually return to the initial wake size and shape. This progression is almost identical to the conditions generated by the 20ms pulse tested in the previous section with mode transition time only varying within 20ms. The only clear

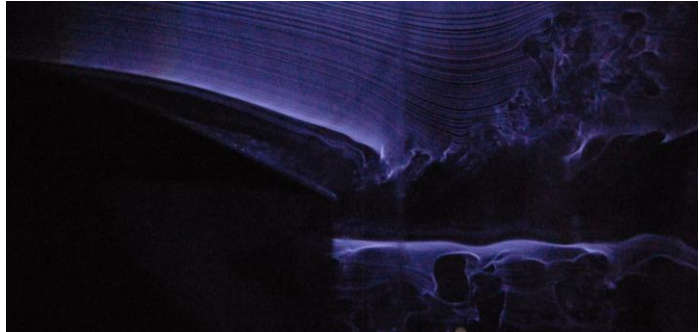


Figure 4.23 Flow conditions after the 20ms pulse passes the airfoil. Note flow continuing to curve downward behind the pulse after passing the

difference is that even 580ms after the pulse passes the usual roughness does not appear in the edges of the wake. Also the shape of the pulse passing the airfoil is a distinct, singular, circular shape that appears to be a rotating vortex directly above the airfoil surface.

The 20 and 30ms pulses both generate completely attached flow on the airfoil over 75% of the area usually separated area shown in Figure 4.22. Clearly visible in this shot is the separation of the streamlines as the freestream flow is forced down into the boundary layer when the pulse

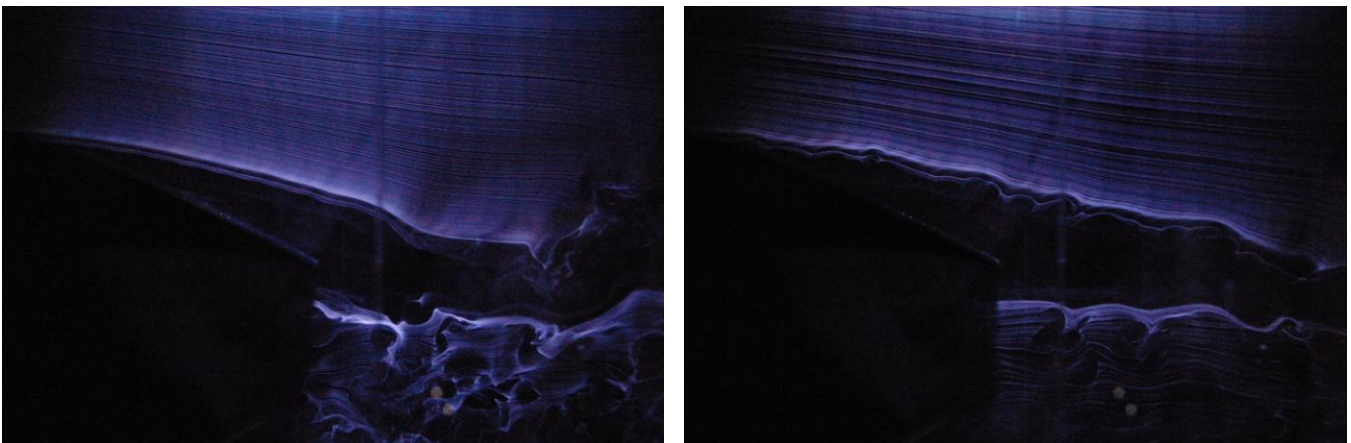


Figure 4.24 (left) Stable wake position 100ms after 20ms configuration 4 pulse. Note mean wake position below airfoil position and clear unsteady areas in the far right of the shot generated after the pulse passes the airfoil. The disturbance in the far right of the shot is not the pulse, but a remnant of this disturbance.

Figure 4.25 (right) Flow 320ms after the 20ms pulse passes the airfoil. Note the upper flow stream still has a downward slope indicating continued circulation and decreasing the overall size of the

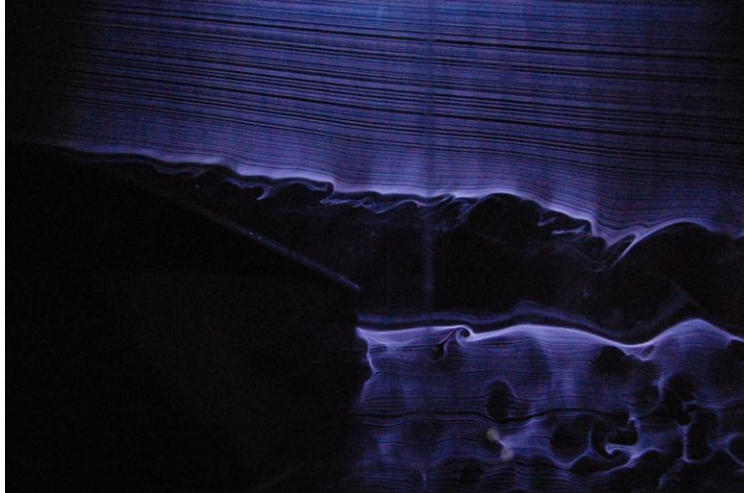


Figure 4.26 Trailing edge vortices begin to appear in the wake 500 ms after the pulse eventually leading to full wake size.

shown in Figure 4.24. In this case the wake size is smaller than that shown in previous tests and continued circulation after the airfoil surface makes the center of the wake below the trailing edge. The flow continues like this for another 50ms at which point the mean wake begins to move up to be even with the airfoil. However as can be seen in Figure 4.25 the flow stream above the airfoil continues to show a downward slope until 400ms after the pulse passes when the wake becomes straight, but somewhat smaller than the uncontrolled flow wake. This smaller

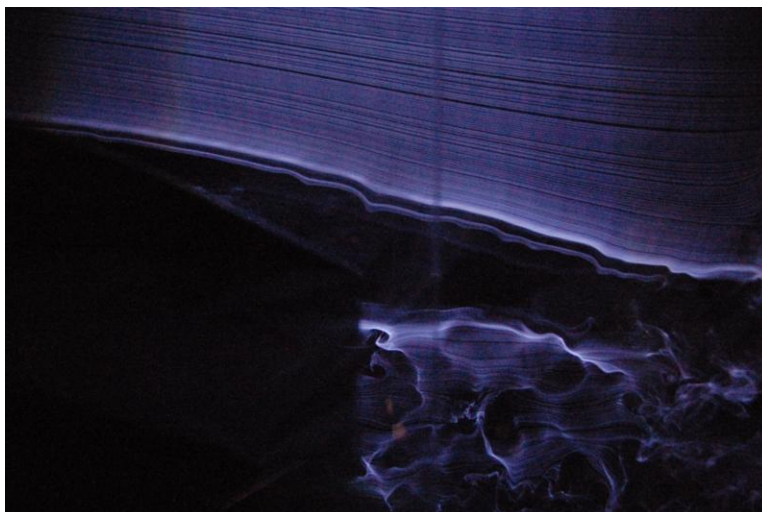


Figure 4.27 Flow 170ms after the 30ms pulse passes the airfoil. Note very small wake that is inclined downwards. This flow regime continues for 200 ms after the pulse.

passes. The 20ms flow does not completely re-attach the flow to the trailing edge of the airfoil, however after the pulse passes the trailing edge the flow continues to circulate around the airfoil, with a much smaller separation zone shown by the 10ms pulse or other previous tests of impinging jets (Figure 4.23).

100ms after the pulse completely passes the airfoil the wake stabilizes (after a period of fluctuation) as

size continues another 100ms until vortices begin to appear in the wake (Figure 4.26) and it returns to normal size about 50ms later. The vortex caused by the 20 and 30ms puff clear in Figure 4.23 is very similar in shape to that caused by the 10ms pulse, but is larger proportional to the duration of the puff. This vortex is defined and appears to be rotating about the z-axis.

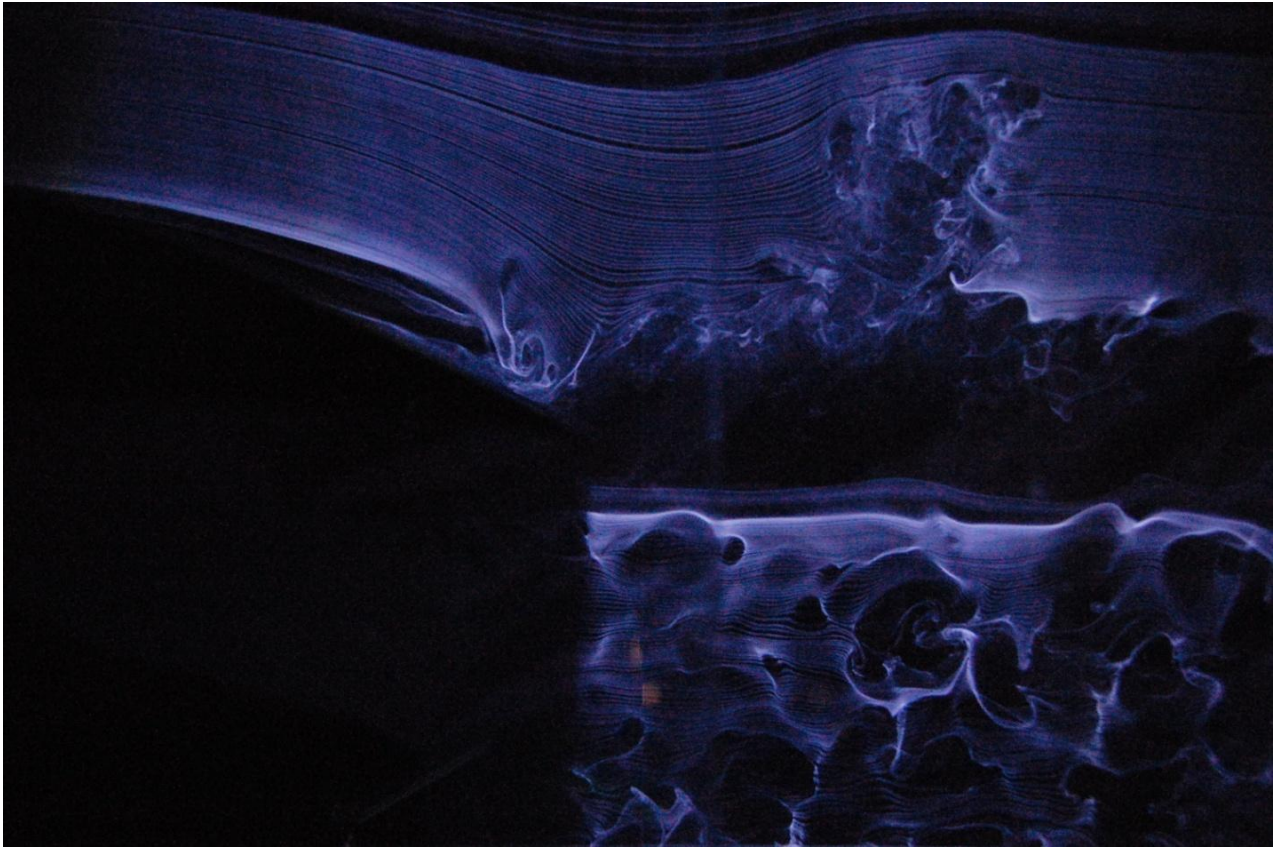


Figure 4.28 Reattached flow immediately after a 30ms pulse impinging at 22.5 degrees at the leading edge.

Unlike all other tests excepting the 10ms streamwise pulse (Figure 4.5) the 30ms pulse directed at 22.5 degrees from the freestream is able to reattach the flow to the trailing edge, with a separation bubble starting at the usual separation point (Figure 4.28). This area of fluid directly upstream of the pulse never separates from the airfoil, and separation at the trailing edge is maintained for 50ms after the pulse vortex passes. For 200ms after the pulse passes the airfoil it is able to maintain a very small wake that is sloped significantly downward showing clear circulation and lift on the airfoil visible in Figure 4.27. This wake size and shape is very similar if not somewhat smaller than that produced by the 10ms streamwise pulse tested in section 4.1.2. 200ms after the pulse the wake becomes straight behind the airfoil but approximately the same size for another 100ms, then grows gradually, with a few minor vortices until 380ms after the pulse at which point the wake returns to its original size, and by 500ms after the pulse the irregularities in the wake re-appear.

#### 4.1.6 45-Degree impinging jet 1.4 inches behind the leading edge



Figure 4.29 Attached flow over 65% of the airfoil generated by a 10ms pulse 45 degrees 1.4" back along the chord of the airfoil. Note very clear counterclockwise rotation in the pulse vortex.

The 10ms jet impinging aft of the leading edge (configuration 5) initially acts similar to the 20 and 30ms pulses at 22.5 degrees nearer to the leading edge in the previous section. It is able to generate attached flow between 50 and 75% over the usually separated area. The pulse itself clearly visible in Figure 4.29 is very similar to the 10ms pulse at 22.5 degrees at the leading edge (Figure 4.20). The pulse is very clearly defined as a counter

clockwise rotating vortex by its smoke pattern (Figure 4.29). This 10ms pulse is almost able to re-attach the flow at the trailing edge, only achieved with an impinging jet of 30ms (possible with smaller streamwise jets). Additionally after the pulse passes it generates very disturbed wake flow visible in Figure 4.30 similar to the 30ms configuration 4 pulse which eventually leads to a very small sloped wake Figure 4.31. This wake shows clear continued circulation

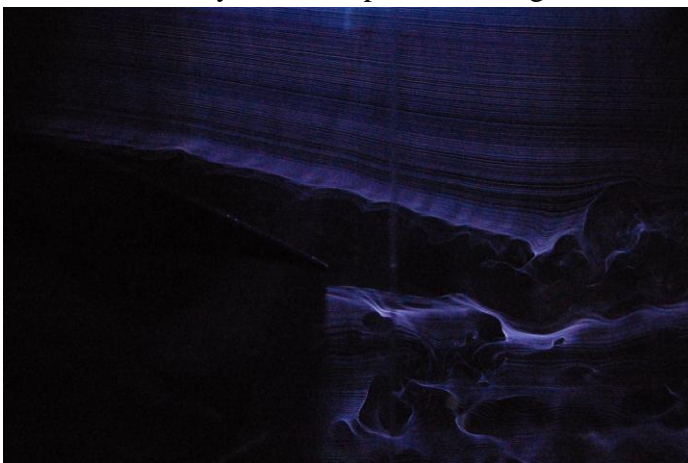


Figure 4.30 Disturbed wake flow 150ms after the 10ms pulse passed the trailing edge

around the airfoil indicating increased lift generated for 270ms after the pulse when the wake remains small but begins to flow straight aft indicating low drag, but no clear improvement in lift. This decrease in wake size begins to breakdown in the form of wake vortices (Figure 4.32) around 350ms after the pulse which lead to a full wake size returning 450ms after the pulse.

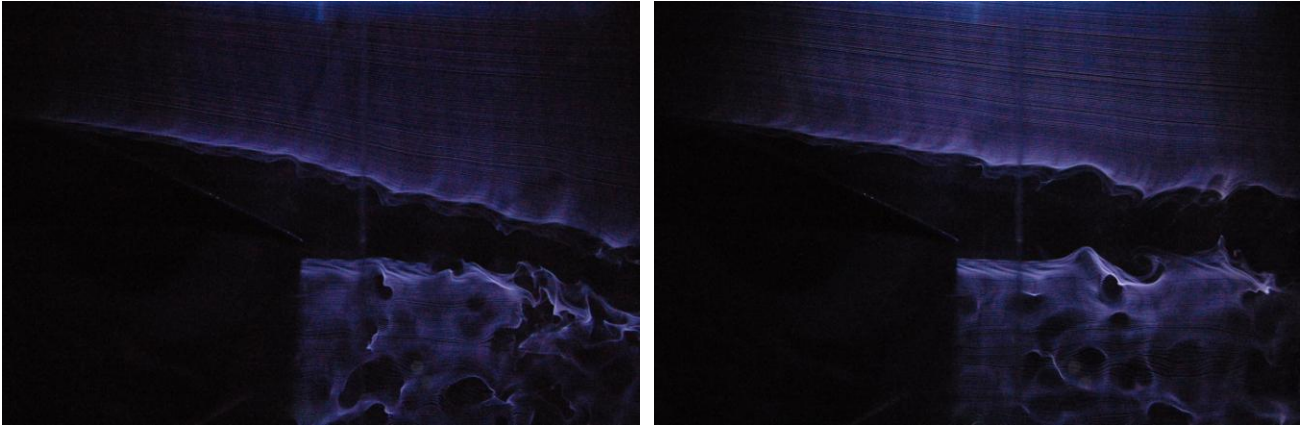
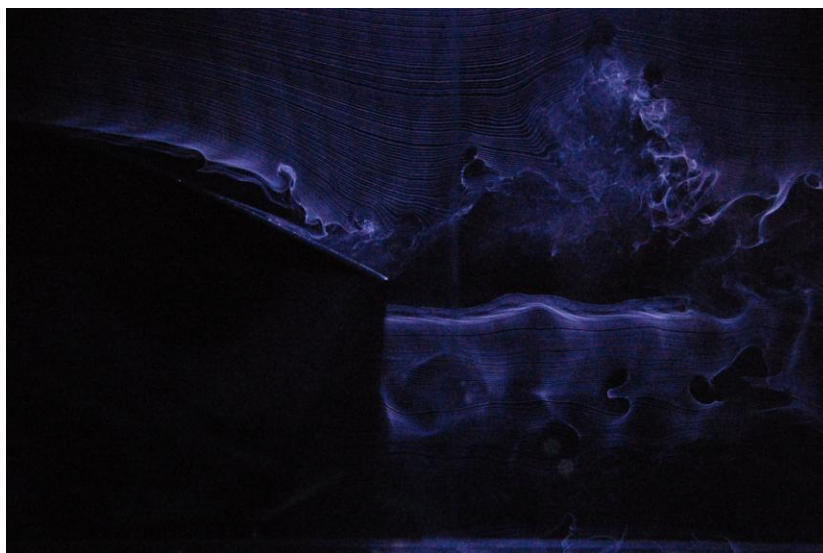


Figure 4.31 Small wake trending downward 200 ms after the 10ms pulse passes the airfoil.  
 Figure 4.32 Flow 350ms after the pulse passes the airfoil. At this point the smaller wake is decaying into the larger and large vortices are being shed into the wake.

The pulse vortex generated by the 20 and 30ms configuration 5 pulses are identical in shape to those shown for the 10ms pulse (Figure 4.29), except proportionally larger depending



on pulse duration. The 20ms pulse is able to create attached flow over 90% of the separated portion immediately behind the pulse, after the pulse passes the last 25% of the foil remains attached aft of a separation bubble, shown in Figure 4.33. This attachment at the trailing edge remains for

Figure 4.33 20ms flow generated from configuration 5 note separation bubble followed by final 25% of airfoil completely attached.

30ms until it finally separates. After the flow separates from the airfoil it generates a very large vortex behind the trailing edge shown in Figure 4.34. This leads to an unstable period in the wake that continues for 200ms until it finally settles as a clean wake trending downward as seen in Figure 4.35. This flow regime slowly moves up until it is directly downstream of the airfoil, then begins to expand to the full wake size of the initial flow 510ms after the pulse passes the airfoil.

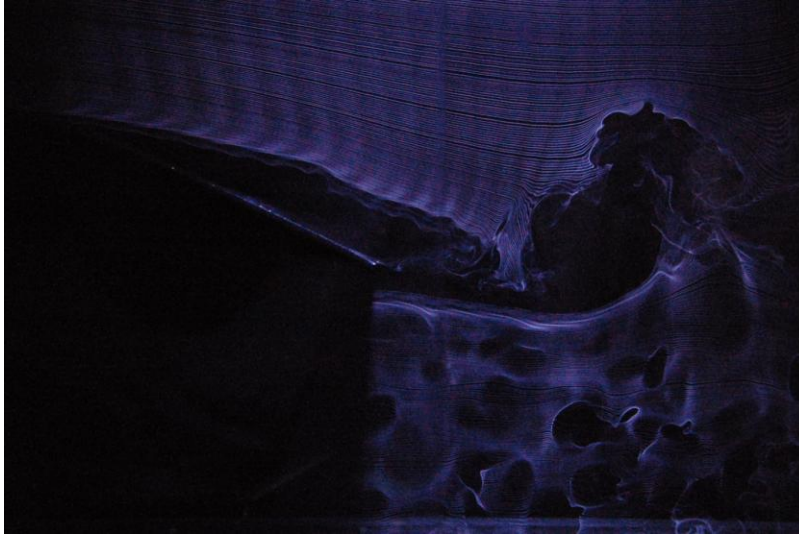


Figure 4.34 Large vortices produced after flow separates from airfoil 100ms after the pulse passes by the foil. Puff vortex is out of frame, and the large vortex apparent is caused after the separation.

The 30ms pulse is able to generate 100% attachment on the trailing edge as can be seen in Figure 4.36. Additionally in this image it is clear that the flow is being pulled down to the trailing edge after the pulse passes since the streamlines in the smoke spread immediately above the usually separated portion of the airfoil. The flow is able to remain fully attached for 20ms then a separation bubble grows and the flow is

completely separated 60ms after the pulse passes. After the flow separates there is enough energy and circulation to keep the flow returning completely behind the airfoil, resulting in almost no wake for another 50ms as shown in Figure 4.37. Contrary to all previous tests there are no vortices generated after the pulse passes the airfoil, after which the flow reaches a steady wake formation. Instead in this test the top edge of the wake smoothly transitioned to a clean downward sloping line 200ms after the pulse passes the trailing edge shown in Figure 4.38. This general size and shape is maintained for another 100ms when the wake size increases and begins to flow straight aft. 350ms after the pulse passes the airfoil vortices begin to appear and the wake rapidly returns to its original size and shape.

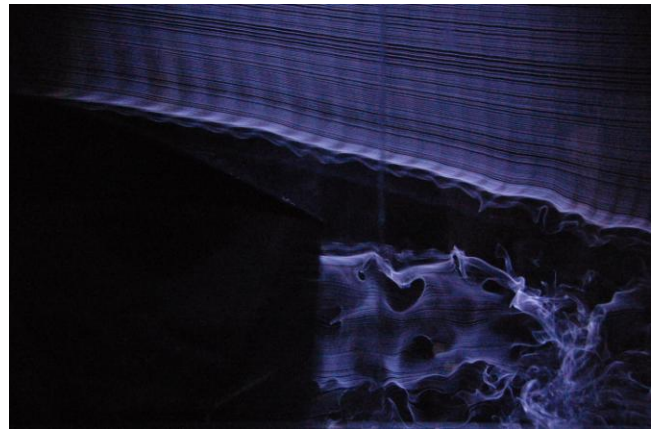


Figure 4.35 Final settling position of wake after vortices caused by the pulse and resulting separation pass. It is smaller and rotated downward as compared to the uncontrolled wake.

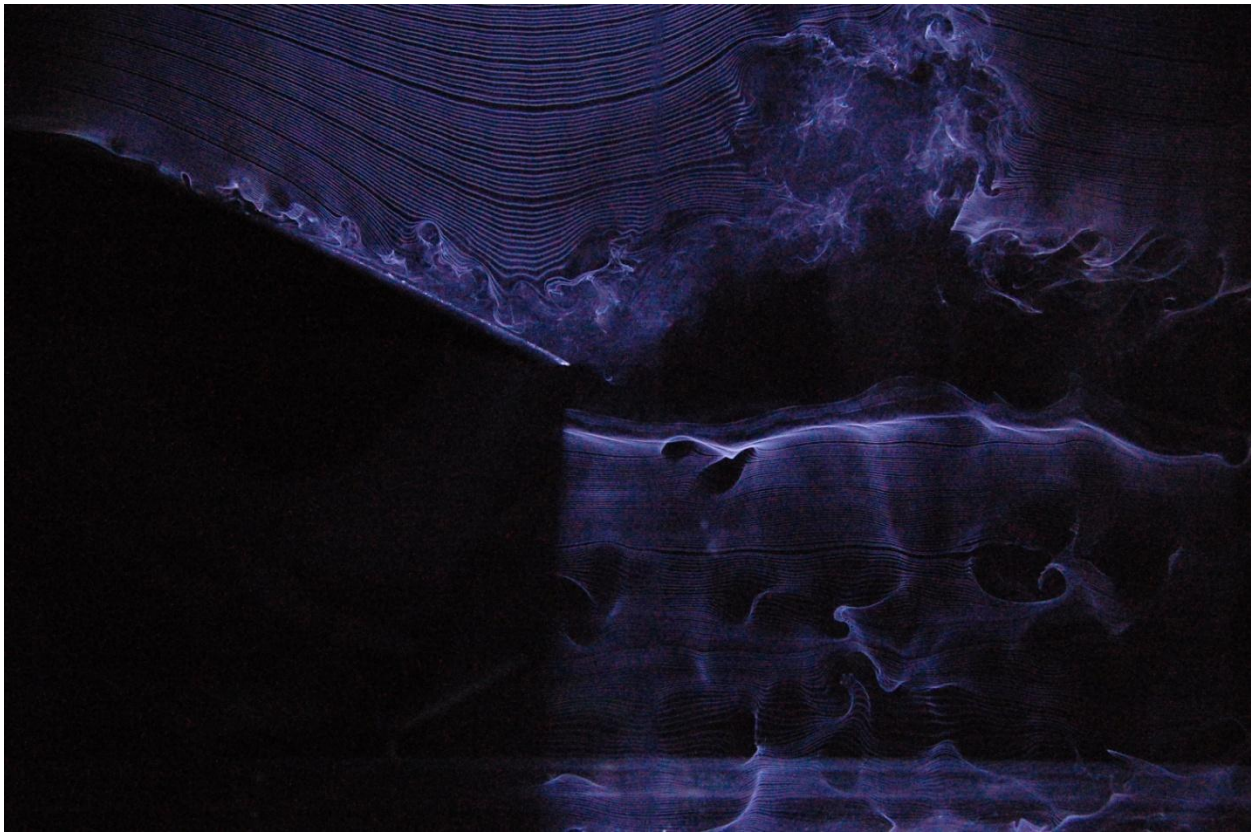


Figure 4.36 Fully attached flow generated by a 30ms jet pulse impinging 1.4 inches back from the leading edge.

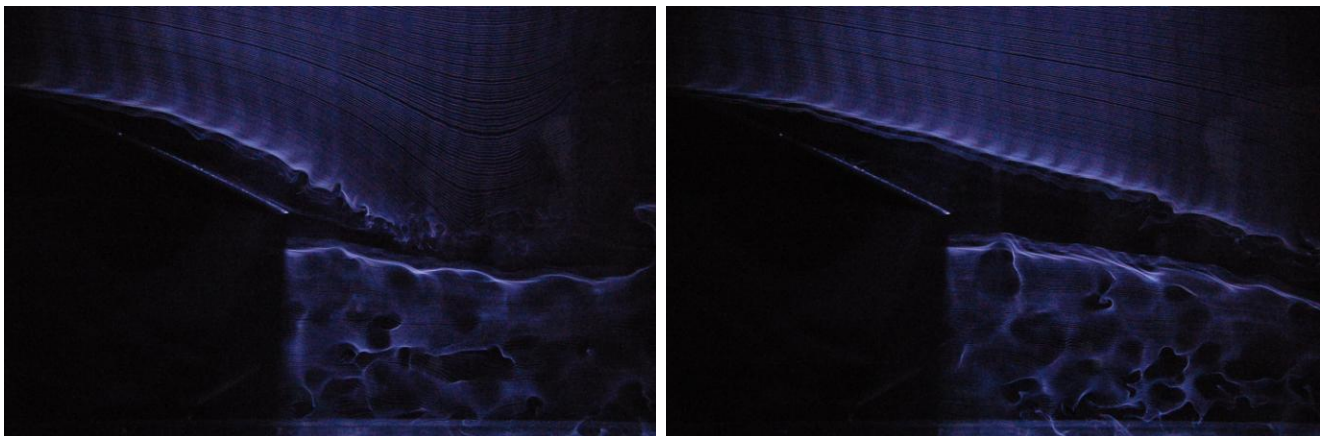


Figure 4.37 Conditions immediately after the flow separates from the airfoil. Note all of the flow rotating completely around the airfoil generating almost no wake.

Figure 4.38 Steady flow stream 190ms after the pulse passes. Characteristic small sloped wake behind airfoil.

## 4.2 Quantitative Comparison

Using an image processing program written in National Instruments® LabVIEW® the size of the wake generated by the airfoil was measured and compared directly to the wake size without flow

control as described in section 3.7. The wake was measured as the vertical distance between smoke lines in the pictures. Using this method charts were generated of the dimensionless wake size ratio, defined as wake height with control divided by height without control, to time after pulse, defined as the total amount of time after the pulse passes the trailing edge of the airfoil (in ms). The wake data received from image processing was plotted, and a simple linear regression was performed on all of the data sets. A plot showing the linear regression of all tests is given in Figure 4.39.

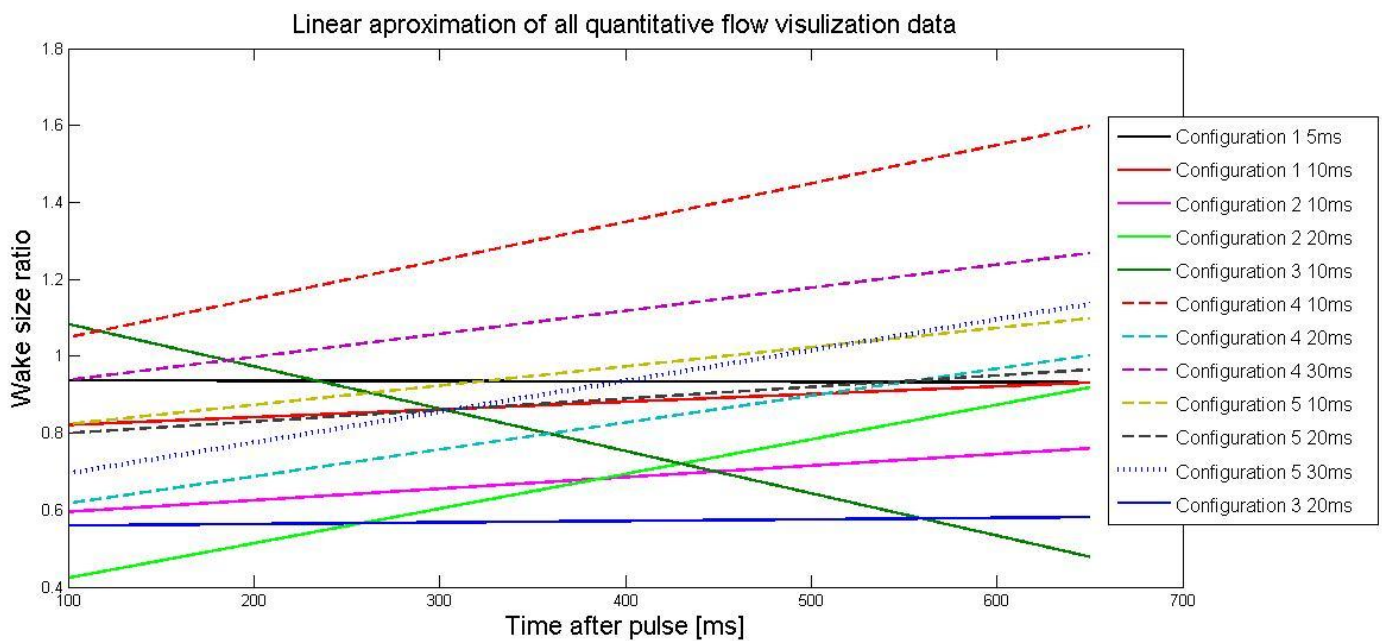


Figure 4.39 Linear Regression of all of the wake size data from image processing. Note several outliers with high (>1) or very low (<.5) wake size. Also single data set with backwards slope. Configuration number key given in section 3.1.

From this image it is clear that while in several cases the image processing software was able to accurately measure the wake size there are several outliers with measured data that does not make sense given the context. The first of these is the 10ms pulse from configuration 3. This is the only line with a downward slope indicating that the mean wake size decreases significantly the longer after the pulse. The likely cause for this error is that there were only 4 data points taken that were able to be analyzed by software. Therefore small measurement error within the software, or eddies appearing in the flow would greatly disrupt the result. In fact this agrees with the qualitative outcome discussed in section 4.1.4 that noted large scale eddies and low

frequency variation within the measured range of this data (90-240ms) after the pulse passes the airfoil visible in Figure 4.15. The 20ms pulse from configuration 2 also suffers from the lack of data with only four data points spread between 100 and 210ms. 10 and 30ms pulses from configuration four appear to have negative flow control, showing larger wakes with control than without. This demonstrates a true error in the test procedure. While in most of the data sets there are many data points taken from multiple pictures there is only one comparison picture

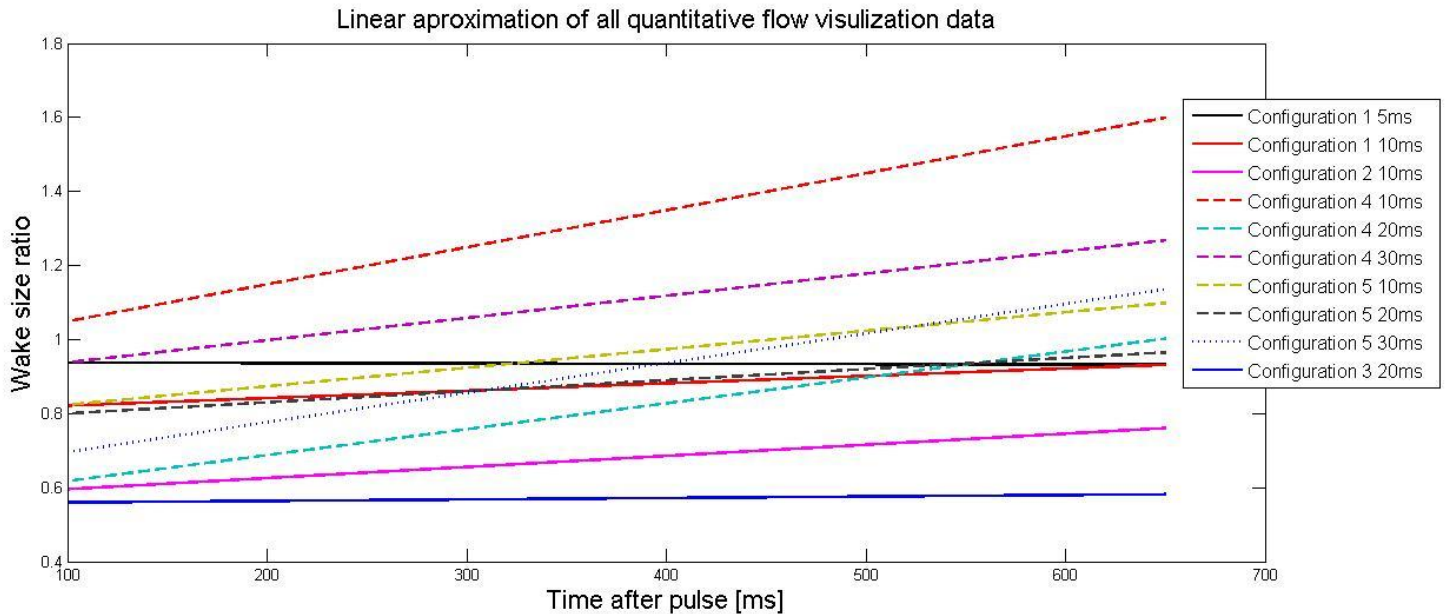


Figure 4.40 Data with outliers removed. Note similar slope over entire range.

with no flow control. Thus if there is any measurement error generated measuring the first picture it is translated into every data point as an error in the y intercept. Thus the slope from these measurements is valuable but the y intercept is not. This effect is also apparent in the 20ms pulse in configuration 2 discussed above. With the major outliers (configuration 2 20ms and configuration 3 10ms) neglected the plot appears as Figure 4.40. Error in measurement also appears in the 20ms pulse for configuration 3 and the 10ms pulse for configuration 2 which appear to have a flat slope but a very low wake size ratio around 0.6. Qualitative picture comparison (section 4.1) rules out this level of efficacy for these tests. Therefore it is more likely that errors were made in the initial measurement and these tests are most likely to have a value that approaches a wake size ratio of 1 (no control effects) as the time after the pulse increases.

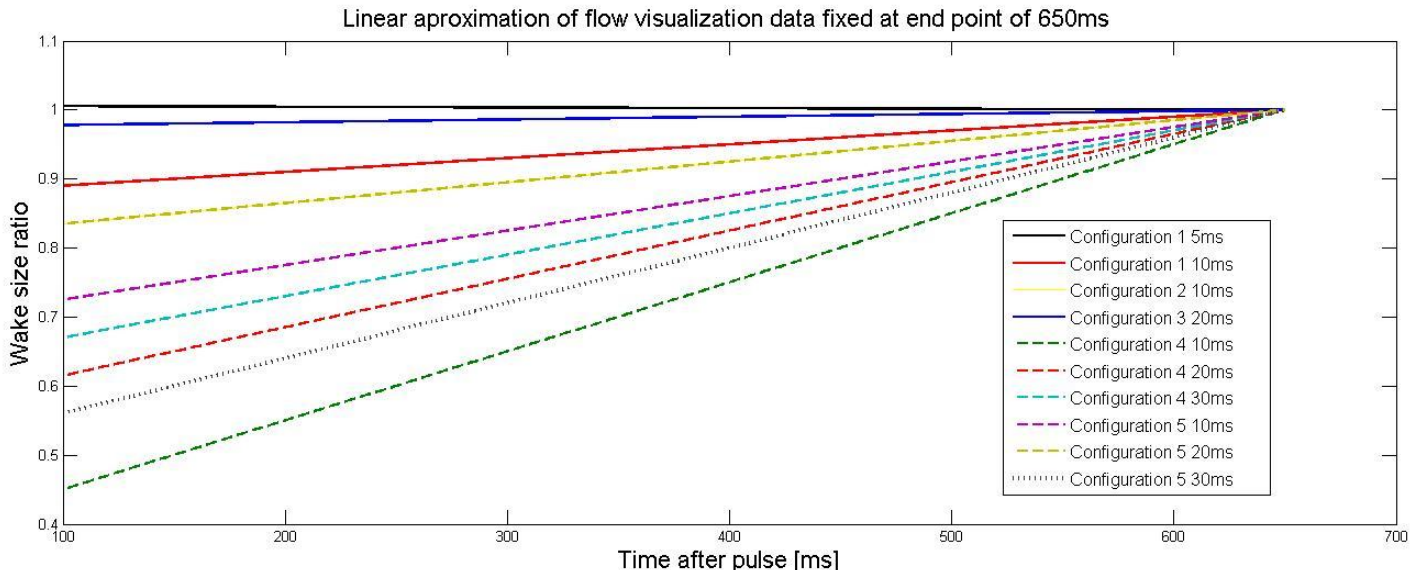


Figure 4.41 Linear approximation of data minus outliers fixed at endpoint to remove error in first measurement.

Artificially setting the wake size ratio to 1 at 650ms after the pulse generates a graph as shown in Figure 4.41. The steepest slope, representing the smallest wake size close to the pulse is attained by the 30ms pulse from configuration 5 and the 10 ms pulse from configuration 4. Further investigation of the data shows that the scatter plot for configuration 4 at 10ms has two significant outlier data points seen in Figure 4.42. These outliers are likely caused by a large scale eddy in the wake at this time point, or significant measurement error in the smoke flow. Removal of these points results in a new linear slope of .0006 a 40% change in the slope estimate. Re-plotting the results makes the data set shown in Figure 4.41 compress even further into Figure 4.43 with the 30ms pulse from configuration 5 showing the most wake reduction as expected from qualitative analysis.

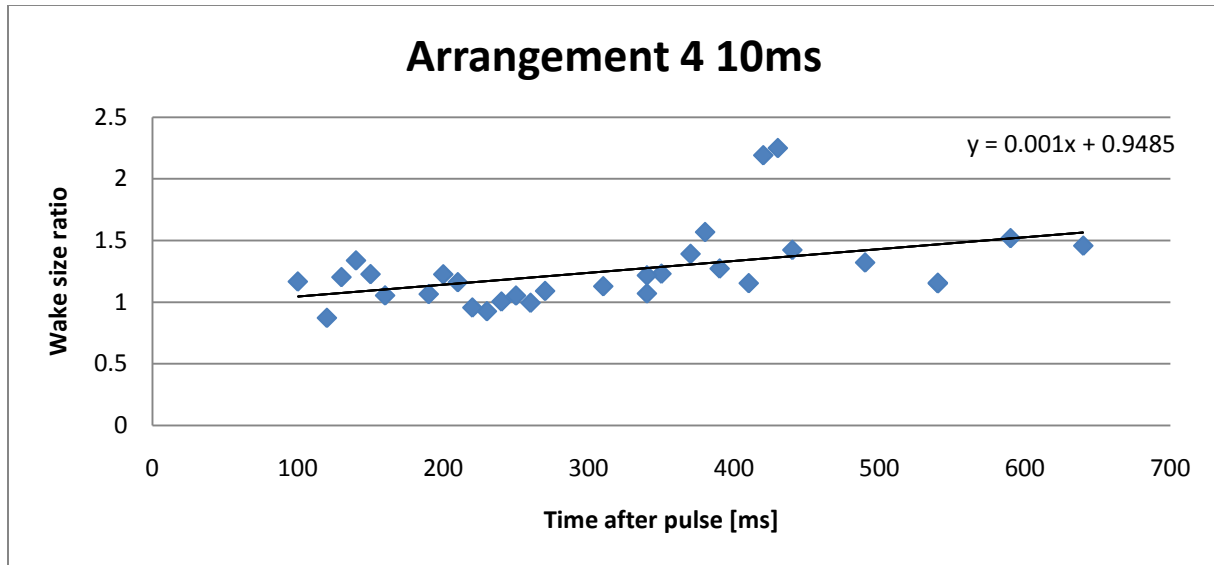


Figure 4.42 Scatter plot with linear regression of a 10ms pulse through configuration 4. Notice good linear fit except for two significant outliers at 450ms.

With the exception of the 30ms pulse from configuration 5 all of the data sets appear to fit the linear approximation well, demonstrating that the figures discussed above are good representations of the flow. In the case of the 30ms pulse from configuration 5 the complete attachment shown in section 4.1.6 and Figure 4.36 results in very small wake size measurements very soon after the pulse passes. This results in a curved shape with no control in the later pulse values, but very small wake sizes produced immediately after the pulse shown in Figure 4.44.

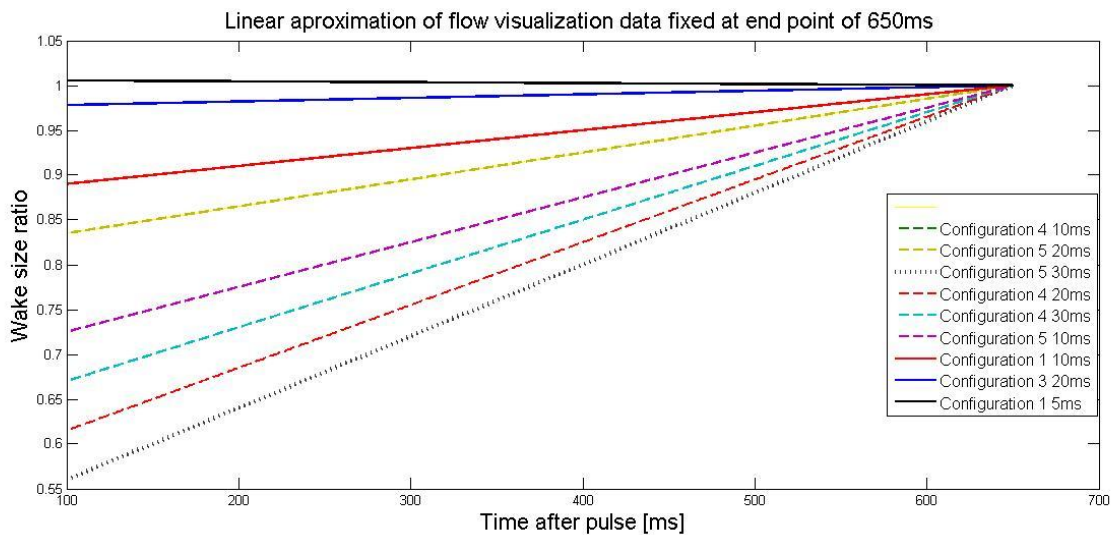


Figure 4.43 Flow visualization data from figure 5.40 but with outliers removed from configuration 4 10ms pulse making it lie directly under the 30ms pulse.

The results generated from the image analysis of the flow visualization had some error due to methodology, and in some cases lack of data, however with proper manipulation high quality

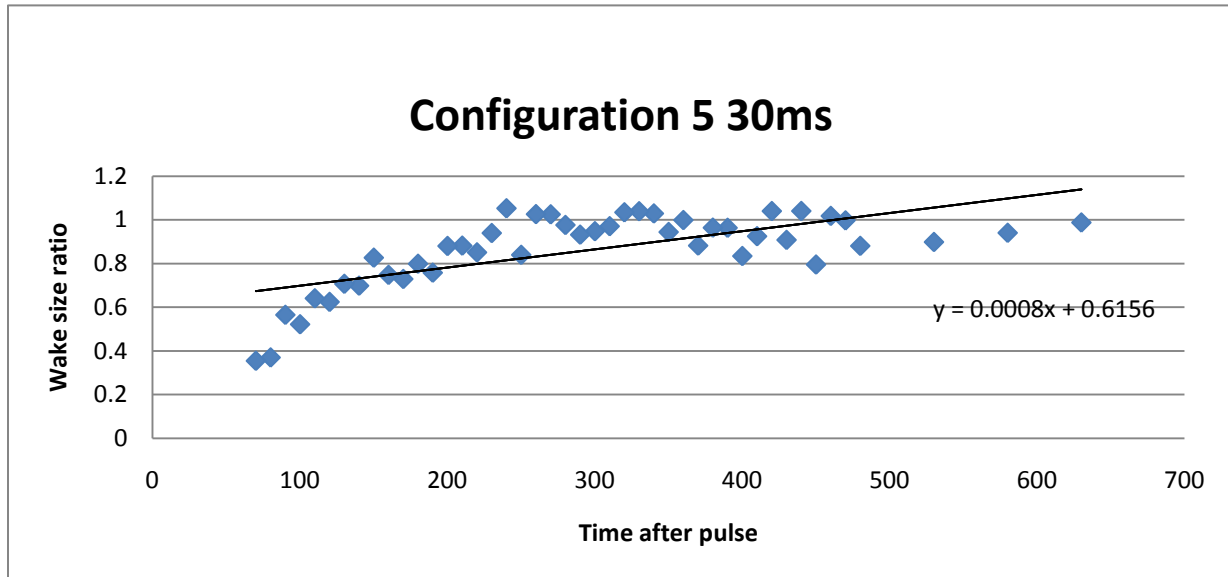


Figure 4.44 Scatter plot of a 30ms pulse from configuration 5. Note very low wake ratios soon after the pulse resulting in overall curved plot shape asymptotically approaching initial flow conditions.

results were achieved, which compared directly with the qualitative analysis performed above.

In many cases the qualitative comparison of images and the quantitative data attained from the image processing software contradict each other in their outcome. The qualitative comparison is very good at checking the amount of attached flow, the shape and immediate effect of the pulse, and the existence of any vortices shed by the airfoil. On the contrary qualitative comparison of wake size a significant time after the pulse is difficult. Quantitative analysis is useless while the pulse is in the frame of the image, since the pulse itself skews the wake size measurement, and cannot make any direct judgment about the attachment. Quantitative wake size measurements after the pulse passes however are much more accurate than qualitative wake comparison. Therefore the qualitative results yield high quality information regarding the pulse and can be used for information shortly after the pulse passes, but quantitative comparison yields much more informative results for long durations after the pulse passes the airfoil, and for long term wake size effects.

## 6.0 CONCLUSION

Flow visualization was performed on a NLF(2)-0415 natural laminar flow airfoil using a smoke wire at flow velocity  $U_\infty = 1.4\text{m/s}$ , Reynolds Number of 27,000 at an angle of attack  $\alpha = 8^\circ$ . At these conditions the airfoil was acting in a low efficiency stalled regime with the flow over the final third of the airfoil completely separated. Using flow visualization the effect of various impinging jets were tested for their ability to re-attach the flow to the trailing edge of the airfoil. Pulsed impinging jets were tested at 100psi and for durations between 10 and 30ms and compared to the flow conditions generated without flow control, and with the more traditional streamwise pulsed jet. High quality images were taken of the separated portion of the airfoil at 10ms intervals from when the jet pulse entered the view frame until approximately 650ms after the pulse had passed the trailing edge. From these pictures qualitative comparisons of the effect of the method on separation could be made. Additionally image processing software was used to quantitatively measure the size of the wake behind the airfoil to estimate the drag reduction effect from each configuration.

From these tests it is clear that configuration four and five, impinging jets at 22.5 degrees located at the leading edge and 45 degrees 1.5 inches behind the leading edge were the most effective methods of flow control. These two configurations, however, have very different effects. Configuration five is the most effective at achieving attached flow immediately after the pulse with the 30ms pulse generating complete attachment and the 20ms pulse generating 90% attachment. Complete attachment created with the 30ms pulse produces a very small wake initially. This effect causes the minimum wake ratio value for this control method very close to the passing of the pulse. However the linear fit used for direct comparison between the control methods does not properly take into account the curve of the measured data. In fact the method is very effective at small times after the pulse passes, but rapidly returns to the initial wake size. In contrast configuration four does not achieve complete attachment to the trailing edge, but the measured wake size is perfectly linear for all pulse durations. Therefore, it generates a much larger decrease in wake size over the majority of the tested time frame. This conclusion is further supported since the slopes of all durations tested for configuration four are steeper than the 10 and 20ms results from configuration five.

Configuration five should be used if very high increases in lift and decreases in drag are necessary, with a very high pulse duty cycle such that the flow remains permanently attached to the airfoil. Configuration four, on the other hand could be used with much less energy input by implementing a shorter pulse duration and lower duty cycle to generate a significant but not as extreme decrease in drag. Further research is necessary to determine the exact cause of this difference; one possibility is that the pulses from configuration four are more able to take advantages of instabilities already in the boundary layer, while the closer pulse generated with configuration five is able to directly add more momentum to the flow. This possibility is supported because the flow effects from configuration four are unaffected by pulse duration with the 10ms and 30ms pulse both slightly better than the 20ms pulse. On the contrary the 30ms pulse from configuration five is able to generate impressive attachment effects while the 10 and 20ms pulses are significantly less effective in mitigating wake size and therefore drag. Additionally, the images of configuration four show a much slower decay back into the rough edged wake apparent without control, whereas the flow after the pulse from configuration five very rapidly returned to the irregular wake. Also 45 degree impingement at the leading edge tested with configuration three was unable to generate very meaningful results while the tests performed closer with configuration five were able to impart enough momentum to generate complete attachment.

One major similarity between the two most effective flow control methods, and clearly absent in the least effective methods is a clear defined rotating vortex directly generated by the pulse. This result is consistent with theory and previous research which shows that an organized vortex is necessary to mix the freestream flow into the boundary layer, generating sufficient momentum to maintain attached flow. The vortices in configuration four and five have the most clearly circular rotating structure and this likely results in their maximum effectiveness in flow control.

From the qualitative analysis of the pictures there was a clear effect in the pulse duration on the immediate attachment of the flow to the trailing edge. For all configurations tested, longer pulses clearly achieved higher percentages of attached flow on the airfoil. The quantitative data on wake size taken some time after the pulse passed however, showed a different result. In these cases, such as configuration four where optimal wake size reduction was achieved, the duration of the pulse had very little effect on the reduction of wake size. This

result suggests that for the conditions tested direct injection of momentum had the greatest effect on immediately attaching the flow to the airfoil, but excitation of the boundary layer due to any pulse of sufficient magnitude caused long term drag reduction effects.

This research has shown that pulsed jets impinging on a laminar airfoil are able to attach flow to otherwise stalled portions of the wing. Additionally it has shown that varying the pulse location and orientation varies the type of control achieved, from complete attachment followed by a rapid return to the original state, to a long term wake reduction effect decreasing form drag on the airfoil. These changes are achieved by both the direct addition of momentum to the boundary layer and by generating vortices that mix the boundary layer and free stream to achieve more control effect than available in the pulse itself. Although it was not proven in these experiments the results also suggest that certain pulse orientations take advantage of stabilities already present in the flow to achieve higher levels of mixing and separation control. This drag reduction and increased lift has potential application in increasing the efficiency of aircraft, with economic and environmental benefits. Additionally this system may be usable as high lift devices for laminar flow airfoils allowing large aircraft that previously relied on the attached flow over high angles of attack only achievable with turbulent flow conditions to use laminar flow wings

## **6.1 Future Work**

The flow visualization discussed in this paper was a first step towards researching the efficacy of impinging jets for flow control; however more quantitative work will be necessary in the future to accurately characterize the effects. Most importantly measurement of lift and drag either directly, using a wake rake or more accurate flow visualization such as PIV need to be performed. Additionally, while the tests described above only provided results one inch from the pulse, further experimentation should be performed to test the spanwise effect of the impinging jets. With this information an estimate of the spacing necessary to provide this effect over the entire surface of an airfoil could be determined. Intuitively an impinging jet would spread significantly more in the spanwise direction than tangential jets because as flow impinges on the airfoil it spreads in all directions instead of being directed straight down the chord of the airfoil as with a tangential pulse. Also if the vortices visible in the flow are rotating about the z-axis as expected it is likely that they extend significantly down the span. The size and shape of this

vortex should be analyzed because it defines how far down the span effective boundary layer mixing occurs resulting in improved separation characteristics. Once the overall span of the effect is analyzed, tests should be performed to analyze the interaction of multiple jets on the airfoil to determine if the effect of the injected pulse, or large vortices generated, is enhanced or damped out by a nearby pulse.

## REFERENCES

- [1] Fox, Robert W., Alan T. McDonald, and Philip J. Pritchard. Introduction to Fluid Mechanics. 7th ed. Hoboken, N.J.: Wiley, 2009.
- [2] Eppink, Jenna. Optimization of Transitional Calibration Body for Wind Tunnel Flow Quality Assessment. MS in Mechanical Engineering Tufts University, 2009.
- [3] "Airfoil Investigation Database - Showing NASA/LANGLEY NLF(2)-0415 " 5/2/2010 <<http://www.worldofkrauss.com/foils/922>>.
- [4] Somers, Dan M. "Design and Experimental Results for a Natural-Laminar-Flow Airfoil for General Aviation Applications." NASA Scientific and Technical Information Branch. NASA Technical Paper 1861 (1981).
- [5] Leinhard IV, John H., and John H. Leinhard V. A Heat Transfer Textbook. 3rd ed. Cambridge, MA: Phlogiston Press, 2008.
- [6] Holmes, B. J., et al. Flight Research on Natural Laminar Flow. Vol. N88-14950. NASA Langley Research Center.
- [7] Fujino, Michimasa, Yuichi Yoshizaki, and Yuichi Kawamura. "Natural-Laminar-Flow Airfoil Development for a Lightweight Business Jet." Journal of Aircraft 40.4 (2003): 609--615.
- [8] Dreese, John "Airfoil Primer - Part 5 " 5/2/2010 <<http://www.dreese.com/primer/airfoil5.html>>.
- [9] Selig, Michael S., Mark D. Maughmer, and Dan M. Somers. "Natural-Laminar-Flow Airfoil for General-Aviation Applications." Journal of Aircraft 32.4 (1995): 710--715.
- [10] Collis, S., et al. "Issues in Active Flow Control: Theory, Control, Simulation, and Experiment." Progress in Aerospace Sciences 40.4-5 (2004): 237-89.
- [11] "1976 CESSNA CARDINAL 177B " 5/2/2010 <<http://axoplasmic.com/Cardinal/main2.html>>.

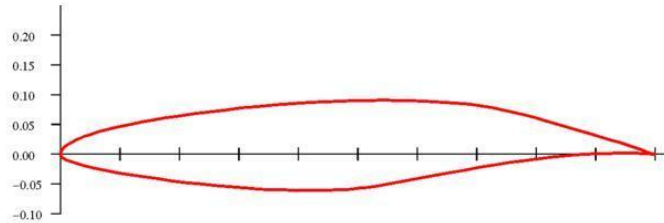
- [12] Magill, John C., and McManus R. Keith. "Exploring the Feasibility of Pulsed Jet Separation Control for Aircraft Configurations." Journal of Aircraft 38.1 (2001): 48--56.
- [13] Iaccarino, Gianluna, et al. RANS Simulation of the Separated Flow Over a Bump with Active Control. Stanford University: Center For Turbulence Research, 2003.
- [14] Greenblatt, David, and Israel J. Wygnanski. "The Control of Flow Separation by Periodic Excitation." Progress in Aerospace Sciences 36.7 (2000): 487-545.
- [15] Seifert, Avi, David Greenblatt, and Israel J. Wygnanski. "Active Separation Control: An Overview of Reynolds and Mach Numbers Effects." Aerospace Science and Technology 8.7 (2004): 569-82.
- [16] Lee, Chester, et al. "A Piezoelectrically Actuated Micro Synthetic Jet for Active Flow Control." Sensors and Actuators A: Physical 108.1-3 (2003): 168-74.
- [17] Johnson, Richard W. The Handbook of Fluid Dynamics. Boca Raton, Fla.: CRC Press, 1998.
- [18] Szarko, David James. "Smoke-Wire Visualization of an Oscillating Flow in a Gas Spring." Bachelor of Science in Mechanical Engineering Massachusetts Institute of Technology, 1993.
- [19] "Making Fog Juice " 5/2/2010  
<[http://www.horrorseek.com/home/halloween/wolfstone/Fog/fogjus\\_FogJuice69.html](http://www.horrorseek.com/home/halloween/wolfstone/Fog/fogjus_FogJuice69.html)>.
- [20] "SB-900 AF Speedlight from Nikon " 5/2/2010 <<http://www.nikonusa.com/Find-Your-Nikon/Product/Flashes/4807/SB-900-AF-Speedlight.html>>.
- [21] "Prism Science Works " 5/2/2010 <[http://prismscience.com/spot\\_specs.php](http://prismscience.com/spot_specs.php)>.

## ADDITIONAL REFERENCES

- (1) Hong, Guang. "Effectiveness of Micro Synthetic Jet Actuator Enhanced by Flow Instability in Controlling Laminar Separation Caused by Adverse Pressure Gradient." Sensors and Actuators A: Physical 132.2 (2006): 607-15.
- (2) Kim, Sang Hoon, and Chongam Kim. "Separation Control on NACA23012 using Synthetic Jet." Aerospace Science and Technology 13.4-5 (2009): 172-82.
- (3) Scholz, Peter, et al. "Leading Edge Separation Control by Means of Pulsed Jet Actuators." 6/5/2008.
- (4) Shan, Hua, et al. "Numerical Study of Passive and Active Flow Separation Control Over a NACA0012 Airfoil." Computers & Fluids 37.8 (2008): 975-92.
- (5) Somers, Dan M. "Design and Experimental Results for a Natural-Laminar-Flow Airfoil for General Aviation Applications." NASA Scientific and Technical Information Branch. NASA Technical Paper 1861 (1981).
- (6) Yarusevych, S., P. E. Sullivan, and J. G. Kawall. "Airfoil Boundary Layer Separation and Control at Low Reynolds Numbers." Experiments in Fluids 38.4 (2005): 545-7.
- (7) You, D., and P. Moin. "Active Control of Flow Separation Over an Airfoil using Synthetic Jets." Journal of Fluids and Structures 24.8 (2008): 1349-57.

## APPENDIX A – AIRFOIL INFORMATION

# NASA/LANGLEY NLF(2)-0415



## Other Similar Airfoils

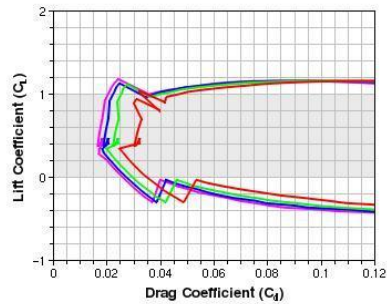
- EPPLER 417 (Compare)
- DFVLR R-4 (Compare)
- EPPLER 403 (Compare)
- naca-2614 (Compare)
- MH 200 12.97% (Compare)
- Apex 16 (normalized using XFOIL date021206) (Compare)
- DORNIER A-5 (Compare)
- NASA/LANGLEY LS(1)-0413 (GA(W)-2) (Compare)
- NACA 67,1-215 (Compare)
- GOE 14K (Compare)

**Thickness:** 15.0%  
**Camber:** 3.0%  
**Trailing edge angle:** 16.2°  
**Lower flatness:** 3.4%  
**Leading edge radius:** 0.9%

**Max  $C_L$ :** 1.175  
**Max  $C_L$  angle:** 6.0  
**Max L/D:** 49.564  
**Max L/D angle:** 5.0  
**Max L/D  $C_L$ :** 1.084  
**Stall angle:** -0.5  
**Zero-lift angle:** -4.0

## Drag Polar for NASA/LANGLEY NLF(2)-0415

■ Re=25000    ■ Re=50000    ■ Re=75000    ■ Re=100000



## Lift for NASA/LANGLEY NLF(2)-0415

■ Re=25000    ■ Re=50000    ■ Re=75000    ■ Re=100000

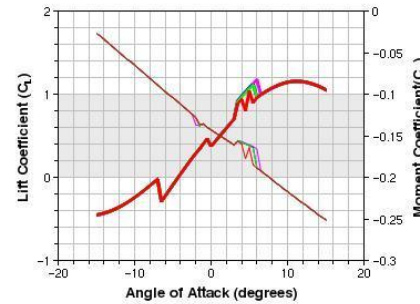


**Figure A.1** Airfoil information for NLF(2)-0415 from the Airfoil Investigation Database [3.1]

## APPENDIX B—AIRFOIL MODEL DRAWINGS

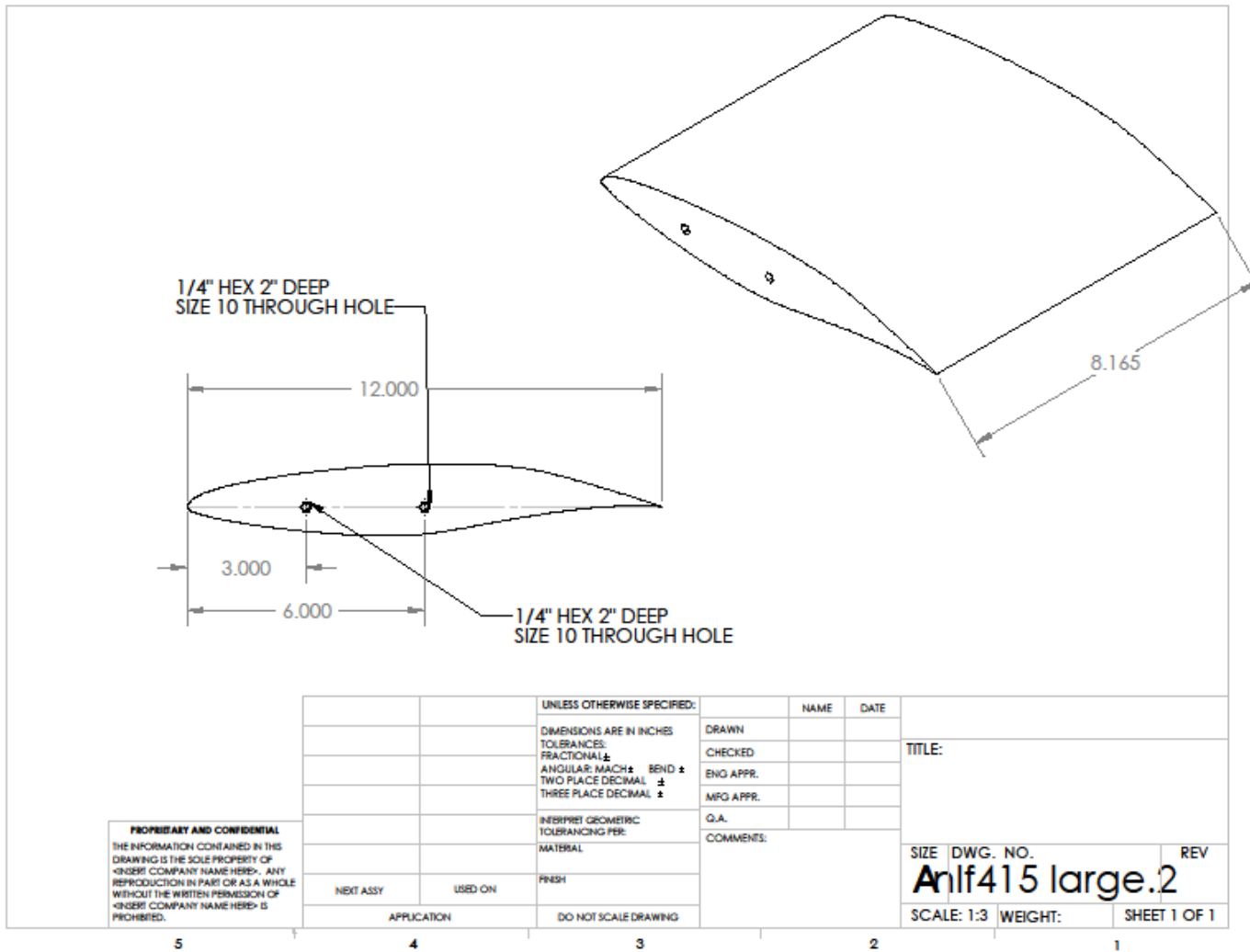


Figure B.1 Technical drawing of large half of test airfoil model

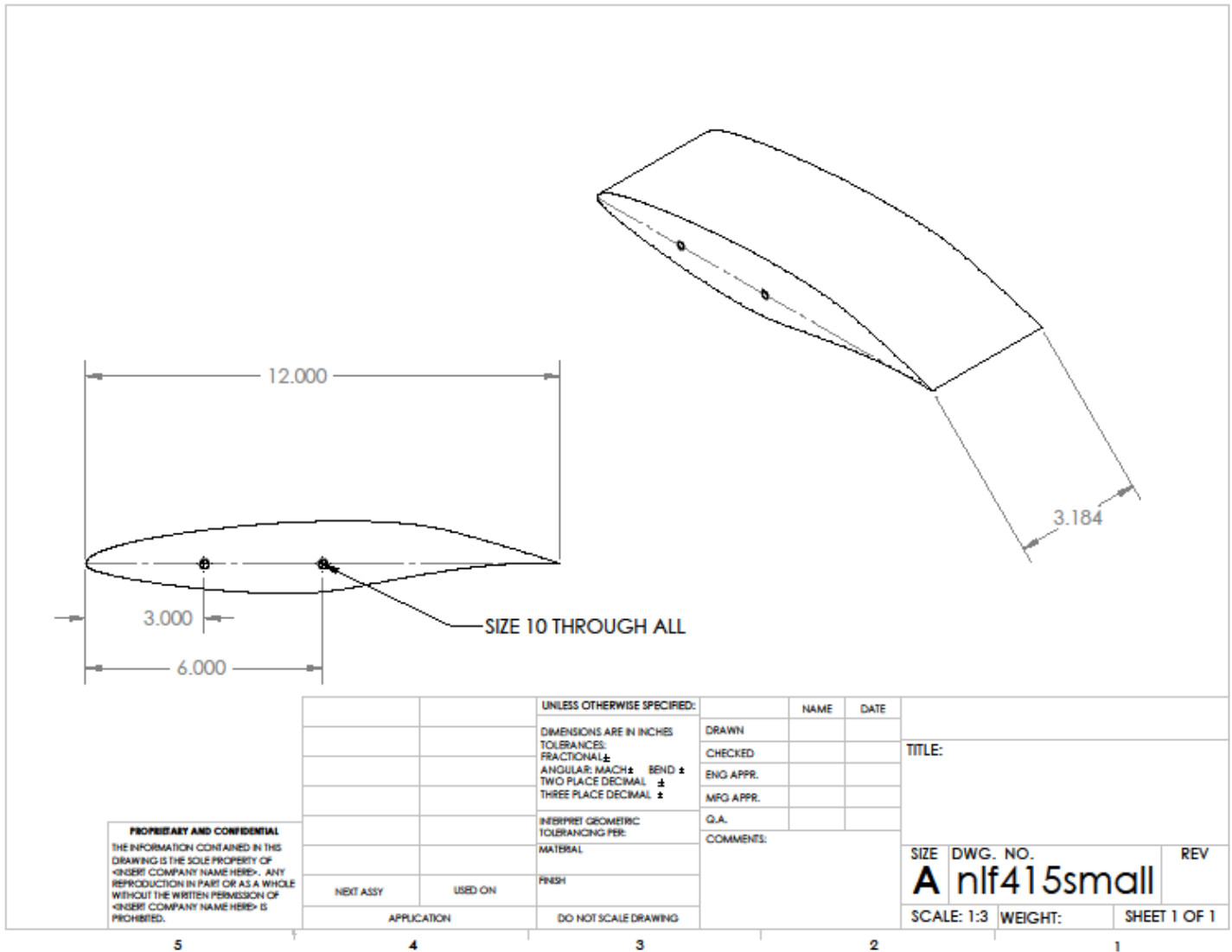


Figure B.2 Technical drawing of small half of test airfoil model

## APPENDIX C—DATA ACQUISITION HARDWARE

# NI 9401

## 8 Ch, 5 V/TTL High-Speed Bidirectional C Series Digital I/O Module



- 8-channel, 100 ns ultrahigh-speed digital I/O
- 5 V/TTL, sinking/sourcing digital I/O
- Bidirectional, configurable by nibble (4 bits)
- Industry-standard 25-pin D-Sub connector
- Hot-swappable operation
- -40 to 70 °C operating range

## Overview

The NI 9401 is an eight-channel, 100 ns bidirectional digital input C Series module for any NI CompactDAQ or CompactRIO chassis. You can configure the direction of the digital lines on the NI 9401 for input or output by nibble (four bits). Thus, you can program the NI 9401 for three configurations – eight digital inputs, eight digital outputs, or four digital inputs and four digital outputs. With reconfigurable I/O (RIO) technology (CompactRIO only), you can use the NI LabVIEW FPGA Module to program the NI 9401 for implementing custom, high-speed counter/timers, digital communication protocols, pulse generation, and much more. Each channel is compatible with 5 V/TTL signals and features 1,000 Vrms transient isolation between the I/O channels and the backplane.

From: National Instruments® <http://sine.ni.com/ds/app/doc/p/id/ds-86/lang/en> see link for more information

# Nikon D40 Camera

## Nikon Digital SLR Camera D40 Specifications

<b>Type of Camera</b>	Single-lens reflex digital camera
<b>Effective Pixels</b>	6.1 million
<b>Image Sensor</b>	RGB CCD, 23.7 x 15.6 mm; total pixels: 6.24 million
<b>Image Size (pixels)</b>	3,008 x 2,000 [L], 2,256 x 1,496 [M], 1,504 x 1,000 [S]
<b>ISO Sensitivity</b>	200 to 1,600 in steps of 1 EV with additional setting one stop over 1600
<b>Storage Media</b>	SD memory card, SDHC compliant
<b>Storage System</b>	Compressed NEF (RAW); 12-bit compression; JPEG; JPEG baseline-compliant
<b>File System</b>	Exif 2.21, Compliant DCF 2.0 and DPOF
<b>White Balance</b>	Auto (TTL white-balance with 420-pixel RGB sensor), six manual modes with fine-tuning and preset white balance
<b>LCD Monitor</b>	2.5-in., 230,000-dot, low-temperature polycrystalline TFT LCD with brightness adjustment
<b>Playback Function</b>	1 frame; Thumbnail (A or 9 segments); Magnifying playback; Slide show; Histogram indication; Highlight point display; Auto image rotation
<b>Delete Function</b>	Card format, All frames delete, Selected frames delete
<b>Video Output Interface</b>	NTSC or PAL
<b>Text Input</b>	Hi-speed USB; Mass Storage and MTP/PTP selectable
<b>Text Input</b>	Up to 36 characters of alphanumeric text input available with LCD monitor and multi-selector; stored in Exif header
<b>Lens Mount</b>	Nikon F mount with AF contacts
<b>Compatible Lenses*</b>	Type G or D AF Nikkor 1) AF-S, AF-I: All functions supported, 2) Other Type G or D AF Nikkor: All functions supported except autofocus, 3) PC Micro-Nikkor 85mm f/2.8D: Can only be used in mode M; all other functions supported except autofocus, 4) Other AF Nikkor**7A/P Nikkor: All functions supported except autofocus and 3D Color Matrix Metering II, 5) Non-CPU: Can be used in mode M, but exposure meter does not function; electronic range finder can be used if maximum aperture is f5.6 or faster *1. IX Nikkor lenses can not be used *2. Excluding lenses for F3A
<b>Picture Angle</b>	Equivalent in 35mm [1/35] format is approx. 1.5 times lens focal length
<b>Viewfinder</b>	Fixed-eyelevel pentaprism mirror type; built-in diopter adjustment (-1.7 to +0.5m <sup>-1</sup> )
<b>Eyepoint</b>	18mm (-1.0m <sup>-1</sup> )
<b>Focusing Screen</b>	Type B BriteView Clear Matte screen Mark V with superimposed focus brackets
<b>Viewfinder Frame Coverage</b>	Approx. 95% (vertical/horizontal)
<b>Viewfinder Magnification</b>	Approx. 0.6x with 50mm lens at infinity (-1.0m <sup>-1</sup> )
<b>Viewfinder Information</b>	Focus indications, AF lock indicator, Shutter speed, Aperture value, Exposure/Exposure compensation indicator, Exposure mode, Flash output level compensation, Exposure compensation, Number of remaining exposures, Flash-ready indicator
<b>Autofocus</b>	TTL phase detection by Nikon Multi-CAM 530 autofocus module with AF-assist range approximately 1ft. 8in.-9ft. 10in.; Detection range: -1 to +19 EV (ISO 100 at 68°F)
<b>Lens Servo</b>	1) Autofocus (AF): Instant single-servo AF (AF-S); continuous servo AF (AF-C); auto AF-S/AF-C selection (AF-A); predictive focus tracking automatically activated according to subject status, 2) Manual focus (M)
<b>Focus Area</b>	Can be selected from 3 focus areas
<b>AF Area Modes</b>	1) Single Area AF, 2) Dynamic Area AF, 3) Dynamic Area AF with Closest Subject Priority
<b>Focus Lock</b>	Focus can be locked by pressing shutter-release button halfway (single-servo AF) or by pressing AE-L/AF-L button
<b>Exposure Metering System</b>	TTL full-aperture exposure metering system 1) 3D Color Matrix Metering II (type G and D lenses); Color Matrix Metering II (other CPU lenses); metering performed by 420-segment RGB sensor 2) Center-weighted: Weight of 75% given to 8mm circle in center of frame 3) Spot: Meters 3.5mm circle (about 2.5% of frame) centered on active focus area
<b>Exposure Metering Range</b>	1) 0 to 20 EV (3D Color Matrix or center-weighted metering), 2) 2 to 20 EV (spot metering)
<b>Exposure Modes</b>	Digital Vari Program (Auto), Auto [Flash Off], Portrait, Landscape, Child, Sports, Close Up, Night Portrait Programmed Auto (P) with flexible program; Shutter Priority Auto (S); Aperture Priority Auto (A); Manual (M)
<b>Exposure Compensation</b>	+5 EV in increments of 1/3 EV
<b>Exposure Lock</b>	Exposure locked at detected value with AE-L/AF-L button
<b>Shooting Modes</b>	1) Single frame shooting mode, 2) Continuous shooting mode: approx. 2.5 frames per second, 3) Self-timer mode, 4) Delayed remote mode: 2 s. delay, 5) Quick-response remote mode
<b>Shutter</b>	Combined mechanical and CCD electronic shutter, 30 to 1/4000 s. in steps of 1/3, bulb
<b>Sync Contact</b>	X-contact only; flash synchronization at up to 1/500 s.

<b>Flash Control</b>	1) TTL: TTL flash control by 420-segment RGB sensor; i-TTL: balanced Hi-flash for digital SLR and standard i-TTL: Hi-flash for digital SLR available when CPU lens is used with Built-in Flash, SB-800, SB-600, and SB-400, 2) Auto aperture: Available with SB-800 with CPU lens, 3) Non-TTL: Auto: Available with Speedlights such as SB-800, SB-600, SB-400, 28, 27, and 22s, 4) Range priority manual available with SB-800
<b>Flash Sync Modes</b>	Auto, auto with red-eye reduction; Hi-flash and red-eye reduction available with optional Speedlight Auto, auto slow sync, auto slow sync with red-eye reduction; slow sync and slow sync with red-eye reduction available with optional Speedlight Hi-flash and red-eye reduction available with optional Speedlight Hi-flash, rear-curtain with slow sync; slow sync, slow sync with red-eye reduction, red-eye reduction Hi-flash, rear-curtain sync, red-eye reduction
<b>Built-in Flash</b>	Auto flash with auto pop-up PVS/AM: Manual pop-up with button release Guide number (ISO 200/ISO 100, ft.): approx. 55/39 (manual full 59/42)
<b>Flash Compensation</b>	-3 to +1 EV in increments of 1/3 EV
<b>Accessory Shoe</b>	Standard ISO hot-shoe contact with sync, signal, and ground contacts and safety lock
<b>Self-timer</b>	Electronically controlled timer with duration of 2, 5, 10 or 20 s.
<b>Remote Control</b>	Via Wireless Remote Control ML-L3 (optional)
<b>Power Source</b>	One Rechargeable Li-Ion Battery EN-EL9; charging voltage (Quick Charger MH-23): 7.4V DC, AC Adapter EH-5 (available separately; requires optional AC Adapter Connector EP-5) 1/4 in. (ISO 1222)
<b>Tripod Socket</b>	Approx. 5.0 x 2.5 x 3.7 in.
<b>Dimensions (W x D x H)</b>	Approx. 116.1 x 74.0 x 40.0 mm (without battery, memory card or body cap)
<b>Weight</b>	Approx. 116.1 g, without battery, memory card or body cap
<b>Supplied Accessories*</b>	Rechargeable Li-Ion Battery EN-EL9, Quick Charger MH-23, USB Cable UC-E4, PictureProject, Rubber Eyecup DK-16, Camera Strap, Body Cap BF-1A, Eyepiece Cap DK-5, Accessory Shoe Cap BS-1
<b>Optional Accessories</b>	Wireless Remote Control ML-L3, Capture NX, Camera Control Pro, AC Adapter Connector EP-5, AC Adapter EH-5, Video Cable EG-D100, Spare-Soft Case CF-DCL1, Speedlight SB-800/5B-600/5B-400/R1C1

\*Supplied accessories may differ depending on country or area.

The following SD memory cards have been tested and approved for use in the D40:

- Sandisk 64MB, 128MB, 256MB, 512MB, 1GB, 2GB\*, 4GB\*\*
- Toshiba 64MB, 128MB, 256MB, 512MB, 1GB, 2GB\*
- Panasonic 64MB, 128MB, 256MB, 512MB, 1GB, 2GB\*, 4GB\*\*
- Lexar 128MB, 256MB, 512MB, 1GB, 2GB\*

\*1. If card will be used with card reader or other device, check that device supports 2GB and 4GB cards.  
\*2. SDHC compliant. If card will be used with card reader or other device, check that device supports SDHC.

**Memory Card Capacity and Image Quality/Size**

The following table shows the approximate number of pictures that can be stored on a 512MB Panasonic Pro HIGH SPEED memory card at different image quality and size settings.

Image quality	Image size	File size*1	Number of available shots**	Number of consecutive shots available**3
RAW	L	5.0MB	65	5
	M	2.9MB	137	100
	S	0.8MB	503	100
FINE	L	1.5MB	260	100
	M	0.8MB	444	100
	S	0.4MB	839	100
NORMAL	L	0.8MB	503	100
	M	0.4MB	755	100
	S	0.2MB	1200	100
BASIC	L	0.2MB	1200	100
	S	0.1MB	2400	100
RAW+BASIC	L+L	5.8MB**	58	4

\*1. All figures are approximate and assume average file size; actual file size and memory card capacity may vary with scene recorded and make of memory card.  
\*2. Maximum number of frames that can be taken before shooting stops. Actual number of photos that can be taken before buffer fills may vary with make of memory card. Additional photographs can be taken as soon as enough memory is available in buffer.  
\*3. Total file size of NEF (RAW) and JPEG images.

Online Video Tutorial - Digitutor  
[http://www.nikondigitutor.com/index\\_eng.html](http://www.nikondigitutor.com/index_eng.html)

© Macintosh®, Mac OS, and QuickTime are trademarks of Apple Computer, Inc. © Microsoft® and Windows® are registered trademarks of Microsoft Corporation. © The SD logo is a trademark of the SD Card Association. © The SDHC logo is a trademark. © Adobe, Acrobat and Adobe Reader are registered trademarks of Adobe Systems Inc. © PictBridge is a trademark. © All other products and brand names are trademarks or registered trademarks of their respective companies. © Images on LCDs and monitors shown in this brochure are simulated. Specifications and equipment are subject to change without any notice or obligation on the part of the manufacturer. November 2006 ©2006 NIKON INC.

**WARNING** TO ENSURE CORRECT USAGE, READ MANUALS CAREFULLY BEFORE USING YOUR EQUIPMENT. SOME DOCUMENTATION IS SUPPLIED ON CD-ROM ONLY.

**NIKON INC.**  
 1300 Walt Whitman Road, Melville, N.Y.  
 11747-3064, U.S.A.  
[www.nikonusa.com](http://www.nikonusa.com)

Printed in Japan Code No. GC260205 (07030k)



From Nikon [http://www.nikonusa.com/Assets/Digital-SLR/25420-Nikon-D40/PDF/D40\\_Brochure.pdf](http://www.nikonusa.com/Assets/Digital-SLR/25420-Nikon-D40/PDF/D40_Brochure.pdf) see [nikonusa.com](http://www.nikonusa.com) for more information

### SPOT: Specifications

Housed in a 6.7" H 6.7 H 8" enclosure (Fig 1), and weighing in at 10 lbs, SPOT is a compact submicrosecond flash system operating from 120 VAC power. Three trigger inputs are included:

- Manual — push button
- Switch closure — ¼" phone jack
- Pulse (e.g. TTL) — BNC

The stored energy of approximately 8 J is released in a short flash of less than 500 ns. Fig. 2 illustrates FWHM and FW1/3M times for full visible spectrum and for 520 nm line filter. The light collected by a 6" fresnel lens forms a relatively uniform "spot," Fig. 3. The peak intensity of 69 million lumens delivers a pulse having 28.5 beam candlepower-seconds. At 40" from SPOT, the beam diameter is nominally 20" to 24"; however, beam spreads from 14" to 40" can be selected during manufacture. A typical camera setting is f/5.6 to f/8 at 200 ASA for objects illuminated from 3 feet.

The design can be adapted to create different output characteristics for specific applications, such as a 2.7 J pulse with 200 ns FWHM for extremely fast motion, or point sources for shadowgraphs or schlieren images.



Fig. 1: The SPOT Flash.

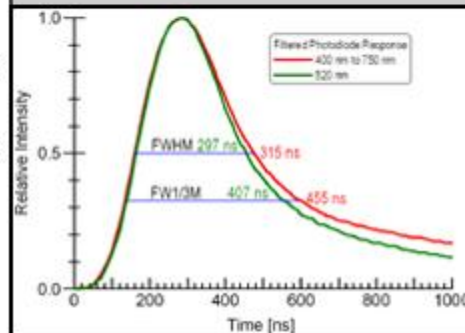


Fig. 2: Temporal Pulse Shape.

[Click here to view full image](#)

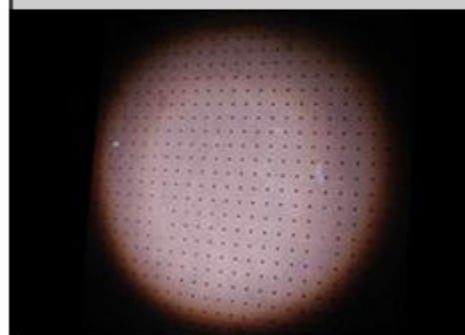


Fig. 3: Illumination Region at 40".

From Prism Science Works [http://prismscience.com/spot\\_specs.php](http://prismscience.com/spot_specs.php)